remote sensing

MDPI

Review

Onboard Lidar Differential Absorption Systems for Greenhouse Gas Sensing: A Review

Oleg A. Romanovskii *, Semyon V. Yakovlev, Sergey A. Sadovnikov, Alexey A. Nevzorov, Aleksey V. Nevzorov, Olga V. Kharchenko and Natalya S. Kravtsova

V.E. Zuev Institute of Atmospheric Optics, 634055 Tomsk, Russia; ysv@iao.ru (S.V.Y.); sadsa@iao.ru (S.A.S.); naa@iao.ru (A.A.N.); nevzorov@iao.ru (A.V.N.); olya@iao.ru (O.V.K.); kravtsova@iao.ru (N.S.K.)
* Correspondence: roa@iao.ru

Highlights

What are the main findings?

- Due to the possible use of onboard equipment in hard-to-reach regions and the full coverage of tropospheric heights during experiments, it is extremely critical to study greenhouse gases using onboard lidar equipment.
- This review systematizes and analyzes the results of the development of onboard mobile lidar differential absorption systems (DIAL and IPDA) for laser remote sensing of major greenhouse gases (H_2O, CO_2, CH_4 and O_3) in the atmosphere in recent years.

What are the implications of the main findings?

- Onboard lidar systems provide, in contrast to standard gas analysis systems, undoubted advantages in quickly obtaining the necessary data in a non-contact way to study the atmosphere's gas composition.
- Onboard DIAL/IPDA lidar systems are capable of large-scale mapping and quantification of the content of major greenhouse gases (H_2O, CO_2, CH_4 and O_3) in the atmosphere of various climate zones.

Abstract

The increase in greenhouse gas concentrations due to natural and anthropogenic impacts is currently considered a determining factor in global warming. This is called the greenhouse effect. In this regard, there is an urgent need to develop effective technologies for the remote monitoring of greenhouse gases with high spatiotemporal resolution and accuracy. Laser remote (lidar) systems provide more accurate measurements of greenhouse gas concentrations in the atmosphere, both natural and anthropogenic. Lidar spectroscopic sensing methods provide, in contrast to standard gas analysis methods, undoubted advantages in quickly obtaining the necessary data in a non-contact way to study the atmosphere's gas composition. There are no reviews of greenhouse gas research using on-board (aircraft-based and space-oriented) differential lidars. This work systematizes and analyzes the results of the development of onboard mobile lidar differential absorption systems for laser remote sensing of major greenhouse gases in the atmosphere in recent years.

Keywords: lidar; DIAL; IPDA; greenhouse gases; airborne; spaceborne

Academic Editor: Carmine Serio

Received: 1 October 2026
Revised: 16 November 2026
Accepted: 24 November 2026
Published: 26 November 2026

Copyright: © 2026 by the authors. Licensee MDPI, Basel, Switzerland. This article is an open access article distributed under the terms and conditions of the Creative Commons Attribution (CC BY) license.

1. Introduction

Currently, one of the most challenging problems identified by the international community as a "major challenge" is global warming and the resulting environmental changes. Predicted forty years ago as a possible response of the natural environment to increasing anthropogenic greenhouse gas emissions [1], global warming has received further confirmation of its unique characteristics in relation to long-term climate fluctuations [2,3]. This confirmation lies in the fact that all previous periods of cooling and warming were regional, while current warming is worldwide. However, there are regions where warming is occurring at a faster rate. These regions include the Arctic, where air temperature increases two to three times faster than elsewhere [4,5].

The increase in greenhouse gas concentrations due to natural and anthropogenic factors is currently considered a major contributor to global warming. This is known as the *greenhouse effect*, which refers to the atmosphere's ability to retain heat emission at the planet's surface. The greenhouse effect leads to an increase in tropospheric temperatures, and a decrease in temperature variations across annual and daily cycles and between the equator and the poles.

Thermal radiation in the Earth's atmosphere is absorbed by greenhouse gas molecules, which consist primarily of polyatomic gases (water vapor, carbon dioxide, ozone, methane, and nitrous oxide). At the same time, there is a lack of research concerning the practical implementation of airborne lidar sounding of nitrous oxide (N_2O). Absorption by greenhouse gas molecules of the thermal radiation quantum part leads to molecular vibrational–rotational excitation, followed by reemission, while part of the reemitted radiation is directed downward. This leads to a decrease in the planet's energy loss due to thermal radiation, i.e., the greenhouse effect is observed. Clouds, which are primarily located in the upper and middle troposphere, contribute to the greenhouse effect on Earth.

In turn, the anthropogenic impact on the Earth's atmosphere leads to a significant increase in CO_2, CH_4 and other greenhouse gas concentrations. As a result, the greenhouse effect increases, which is considered the most significant cause of global warming in the 20th and 21st centuries. If the anthropogenic impact caused by human activity intensifies, it may lead to a further increase in the greenhouse effect. While this may only result in minor temperature changes on a regional scale, it can contribute to permafrost and glacier melting on a global scale. This can result in sea level rise. Therefore, there is an urgent need to develop new technologies for remote monitoring of greenhouse gases with high spatial and temporal resolution and accuracy.

To develop solutions to climate change consequences, it is necessary to provide predictive models with information about greenhouse gas concentrations and distributions in the atmosphere. The development and implementation of new measurement tools, such as laser remote sensing systems, allows for more accurate measurements of the concentrations of both natural and anthropogenic greenhouse gases in the atmosphere.

Lidar (LIght Detection and Ranging) can detect the level of greenhouse gas concentrations, local gas formations, and industrial emission plumes, and identify the presence of elevated levels of organic and other gaseous impurities within them [6–9]. One of the main challenges in implementing lidar gas-analysis systems is the technical complexity of these systems, which must meet strict requirements regarding the stability of radiation characteristics and the ability to adjust laser radiation frequency within the required spectral wavelength range.

It is undeniable that lidar spectroscopic sensing can be used to solve the urgent problem of monitoring the atmosphere. Compared to standard gas analysis methods, it allows for rapid acquisition of data that can be used for studying the composition and physical parameters of the atmosphere without direct contact. For the detection of greenhouse gases in the atmosphere, the infrared (IR) spectrum is of particular interest,

https://doi.org/10.3390/rs18234086

since the vibrational–rotational spectra of the main atmospheric gases exhibit characteristics that facilitate their identification and determination in this range. In particular, the vibrational–rotational spectra of the main greenhouse gas constituents exhibit relatively intense lines and absorption bands in the wavelength range of 1500 to 4000 nm, which corresponds to the near-IR and mid-IR regions of the optical spectrum [6,10]. In this regard, the need to develop differential absorption lidars operating in this wavelength range has increased significantly.

Until now, lidar systems and their applications have been the subject of reviews and monographs published more than 15 years ago [6], have a narrow scope [11–14], or, on the contrary, cover, in addition to differential absorption lidars, other approaches to studying gas components and atmospheric parameters [15–17]. Recent reviews on differential absorption lidars (DIALs) include those on ground-based stationary [18] and mobile [19] lidar systems. There are no reviews of studies of greenhouse gases using differential lidars on board aircraft and spacecraft.

This work systematizes and analyzes the results of the development of onboard mobile DIAL systems for laser remote sensing of the main greenhouse gases in the atmosphere in recent years.

2. Methods and Tools for Greenhouse Gas Analysis

Currently, there are four principal and well-established approaches for the quantitative and qualitative analysis of atmospheric trace gases: local gas analysis instruments, satellite-based active (laser) and passive remote sensing systems, ground-based passive remote sensing systems, and ground- or platform-based lidar/laser remote sensing systems.

A key requirement for remote gas analysis instruments is the ability to operate both day and night, as well as the capacity to measure gas concentrations along various paths. Such functionality is essential for monitoring trace gas emissions over localized areas, where concentrations and dynamics can fluctuate rapidly over short spatial and temporal scales. These requirements cannot be met by local gas analysis instruments [11,20–26], which are limited to single-point measurements, nor by satellite-based systems [27–44], due to their low spatial resolution, the binding of satellite flight coordinates to a specific time and location of the measurements, and passive remote sensing [45–60].

Local gas analysis instruments—such as those from manufacturers Los Gatos Research [11] and Picarro [20–26], which are widely recognized and utilized within the scientific community—rely on a highly sensitive technique that measures the decay of a laser pulse injected into a high-finesse optical cavity filled with an absorbing medium. This technique, known as Cavity Ring-Down Spectroscopy (CRDS), serves as the operating principle for these gas analyzers. The sensitivity of CRDS enables the detection of components at the parts-per-billion (ppb) or parts-per-trillion (ppt) level. CRDS gas analyzers are used for environmental monitoring and specific air quality assessment campaigns, and they also find utility in specialized applications.

It is worth noting that passive remote sensing of greenhouse gases in the Earth's atmosphere is currently well established and implemented through constellations of satellites designed for monitoring purposes [26–44]. These satellites/tools include: Advanced Earth Observing Satellite (ADEOS)/Interferometric Monitor for Greenhouse gases (IMG) instrument (monitoring CH_4, CO_2, and N_2O) [27]; Aqua/Atmospheric Infrared Sounder (AIRS) spectrometer (monitoring CH_4, CO_2, O_3, and CO) [28]; Aura/Tropospheric Emission Spectrometer (TES) (monitoring CH_4, CO_2, and O_3 [29]; Meteorological Operational satellite (MetOp)/Infrared Atmospheric Sounding Interferometer (IASI) spectrometer (monitoring CH_4, CO_2, O_3, H_2O, and N_2O) [30]; Environmental Satellite (Envisat)/SCanning Imaging Absorption SpectroMeter for Atmospheric CHartographY (SCIAMACHY) instrument (monitoring CH_4, O_3, NO_2, CO_2, CO, etc.) [31];

Greenhouse Gases Observing Satellite (GOSAT)/Thermal And Near infrared Sensor for carbon Observations–Fourier Transform Spectrometer (TANSO-FTS) instrument (monitoring CH_4, CO_2) [32,34]; Sentinel-5 Precursor (S5P)/Tropospheric Monitoring Instrument (TROPOMI) instrument (monitoring CH_4, NO_2, SO_2, CO, etc.) [33]; GOSAT-2/TANSO-FTS-2 (monitoring CH_4, CO_2) [34]; GaoFen-5/Greenhouse-gases Monitoring Instrument (GMI) (monitoring CH_4 and CO_2) [35]; Global Observing SATellites for Greenhouse gases and Water cycle (GOSAT-GW)/Total Anthropogenic and Natural emissions mapping SpectrOmeter-3 (TANSO-3) (monitoring CH_4, CO_2, and NO_2) [36]; MethaneSAT (monitoring CH_4) [26]; Sentinel-5/Ultraviolet Visible Near-infrared Shortwave (UVNS) spectrometer (monitoring NO_2, SO_2, CH_4, CO, and H_2CO) [26]; Copernicus Anthropogenic Carbon Dioxide Monitoring (CO_2M) (monitoring CH_4, CO_2, and NO_2) [37].

Preparations are underway for the launch of a satellite equipped with an active remote sensing instrument for methane and other gases [16,26]. This is the Methane Remote Sensing Lidar Mission (MERLIN). The planned launch year is ~2030.

Passive sensing of gaseous pollutant emissions and the measurement of column-averaged concentrations of these gases via the analysis of solar radiation can also be conducted in a monitoring mode using ground-based high-resolution infrared Fourier-transform spectrometers [45–60]. In this configuration, a Fourier-transform spectrometer is paired with a solar tracker, forming a high-precision system for remote atmospheric gas monitoring. The tracker, which utilizes an integrated GPS sensor for precise positioning, automatically follows the sun and directs sunlight into the spectrometer; the latter then measures gas absorption spectra to determine atmospheric composition. It is also worth noting that, within this field of research, the moon can be used as a light source in place of the sun [58]. Such scientific instruments are useful, for example, for measuring atmospheric trace gases at high latitudes, where there are few sunny days per year and polar night prevails for much of the time. Specifically, this type of passive sounding has been implemented using a high-resolution Fourier-transform spectrometer [58] at a research station designed to measure atmospheric trace gases at high latitudes. The spectra obtained can be used to retrieve the concentrations of minor atmospheric constituents in the troposphere and stratosphere. Furthermore, monitoring data from passive atmospheric sounding—collected using a system comprising a Fourier-transform spectrometer and a solar tracker—can be employed to validate satellite-based passive measurements.

As demonstrated in several studies [45–60], Fourier-transform spectrometer–solar tracker systems provide global coverage and monitoring of the total column abundance of atmospheric gases across all latitudes; they are integrated into networks such as NDACC, TCCON, and GAW. Examples include the FTIR spectrometer [45] located at the Polar Environment Atmospheric Research Laboratory (Canada), part of the Network for the Detection of Atmospheric Composition Change (NDACC), which conducts polar measurements from the Arctic to the Antarctic, and the FTS (Fourier Transform Spectroscopy) instrument at the Institute of Atmospheric Optics of the Siberian Branch of the Russian Academy of Sciences (Tomsk, Russia) [46]. Solar trackers and FTIR (Fourier-transform infrared) spectrometers are used within the Total Carbon Column Observing Network (TCCON) [47,50], alongside a mobile FTIR spectrometer [56] employed for the validation of satellite measurements in Karlsruhe, Germany. Other examples include an FTS (Fourier-transform spectrometer) from the NDACC (Network for the Detection of Atmospheric Composition Change) network in Toronto, Canada [48]; an FTIR system in Saint Petersburg, Russia [49]; a solar tracker integrated into an atmospheric gas analysis system in Colorado, USA [51]; solar trackers used with instruments from the NDACC and TCCON networks at stations in New Zealand and Antarctica [52]; an FTIR spec-

trometer at an observatory in Mexico [53]; the FTIR spectrometer at the OASIS (Observations of the Atmosphere by Solar Infrared Spectroscopy) observatory, used to study air composition in the suburbs of Paris, France [54]; an optical solar-tracking system in China [55]; and a solar tracker paired with a Fourier-transform spectrometer in Belgium [57]. The analysis further reveals that Bruker Fourier-transform spectrometers, specifically ultra-high-resolution IR-FTIR instruments, are widely used globally for passive atmospheric sounding and are employed within the NDACC and TCCON networks to analyze atmospheric composition [45,48]. The main drawback of these systems is that it is quite difficult to assess trace gas emissions in small, localized areas and small territories where target gas concentrations fluctuate rapidly within short limits. Measuring trace gas emissions in such locations requires the use of instruments with higher detection limits.

The primary advantages and disadvantages of various approaches to researching atmospheric gaseous pollutants are summarized in Table 1.

Consequently, the development of lidar/laser-based atmospheric gas analysis technologies—which can overcome the aforementioned drawbacks—remains highly relevant and in demand across various sectors, including environmental regulatory bodies and industrial enterprises responsible for anthropogenic atmospheric impact. Another crucial factor is the cross-calibration of measurement results obtained via active gas-analysis systems with those from satellite-based sensors; furthermore, where the sensing path allows, comparisons can be made with data from local gas-analysis instruments installed at the measurement site. Taken together, these measures help improve the accuracy of the data collected.

The use of laser-based remote sensing systems effectively addresses the challenge of atmospheric gas analysis. The development and deployment of new measurement tools enable increasingly precise quantification of atmospheric gas concentrations, whether of natural or anthropogenic origin.

Table 1. Advantages (+) and disadvantages (-) of the research area concerning gaseous impurities in the atmosphere.

Methods for Studying Greenhouse Gases in the Atmosphere			
Local Gas Analysis	**Laser (Active) Sensing**	**Passive Sensing**	**Satellite (Passive and Perspective Active) Sensing**
+ Measurement sensitivity - Performing measurements at a single point	+ Sensing the spatial distribution and integrated content of gaseous impurities over small areas or in hard-to-reach, rugged terrain, with high detection limits + Measuring the concentration of gaseous impurities in various directions - Requirements for the parameters of the laser, receiving optics, and photodetector	+ No need for lasers + Spatial coverage of the sounding area + Spectral sensitivity - Measurement of total column atmospheric content - Measurements impossible at night and difficult under complete cloud cover	+ Spatial coverage of remote sensing - Low spatial resolution - Linking of satellite overpass coordinates to a specific time and location of measurements

3. Differential Absorption Lidar Methods

3.1. DIAL

There are several lidar spectroscopic methods for studying and detecting atmospheric gases, including the DIAL method [6–9]. Based on the resonant absorption of laser radiation by gases, this method has the highest sensitivity for sensing gas components.

As shown in Figure 1, DIAL lidar systems work by absorbing some of the radiation when a pulsed lidar beam passes through a substance under study.

DIAL probes molecules by using two wavelengths (on-line and off-line) of narrow-band laser radiation, one of which is within the maximum absorption band of the studied molecules, while the other lies outside it. The choice of on-line and off-line wavelengths presents several challenges that require a detailed analysis of the absorption spectra of the studied gas, the atmosphere, and any interfering impurities. For the near- and mid-IR range, the spectral gap between on-line and off-line should be ≤5 cm^{-1}, in which case the aerosol scattering cross-section values can be considered sufficiently close, and aerosol scattering can be neglected.

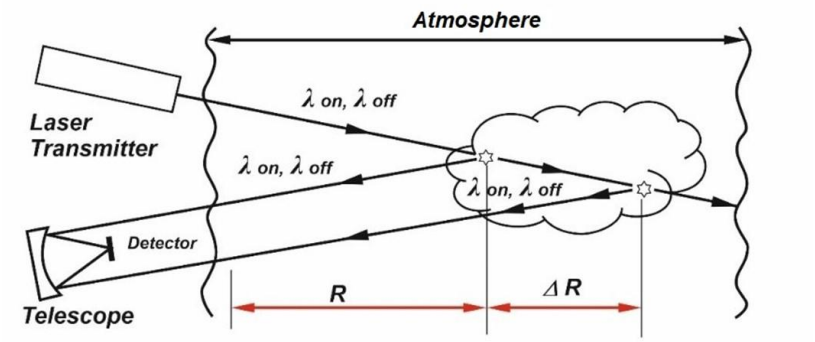


Figure 1. DIAL—differential absorption lidar method.

The time interval between measurements in the center of the line and on its wing should be maintained within a millisecond [61]. By tuning the emission frequency, the first laser pulse is set to the maximum of the absorption line. The second pulse is tuned to the absorption line wing. In this case, spatial resolution and strong backscatter signals are due to large Mie scattering cross-sections. The ratio of the lidar signals provides the required estimate of differential absorption. This makes the DIAL method the most sensitive approach.

The effect of resonance absorption of laser radiation by a studied gas is used in lidar measurements of the concentration profiles of the main greenhouse gases in the atmosphere by the DIAL method. In this case, the concentration of the gas constituent N(R), averaged over the spatial interval ΔR, is defined by the following well-known formula [62,63]:

$$N(R) = \frac{1}{2(K(\nu_{on},R) - K(\nu_{off},R))\Delta R} \ln\left[\frac{P(\nu_{on},R)P(\nu_{off},R+\Delta R)}{P(\nu_{off},R)P(\nu_{on},R+\Delta R)}\right] \quad (1)$$

where $P(\nu_{on},R)$, $P(\nu_{off},R)$, $P(\nu_{on},R+\Delta R)$, and $P(\nu_{off},R+\Delta R)$ are laser signals at the sensing frequencies ν_{on} and ν_{off} returned from the spatial points R and R + ΔR along the sensing path, recorded by the lidar's receiver system; and $K(\nu_{on}, R)$ and $K(\nu_{off}, R)$ are the absorption coefficients along the sensing path at on-line (ν_{on}) and off-line (ν_{off}) frequencies. The profile of the selective absorption line of the studied gas component should be prelimi-

narily calculated using altitude model-based profiles of the atmospheric meteorological parameters. The lidar signals are described using the well-known laser radar equation, which, in the single scattering approximation, can be represented as [62,63]:

$$P(\nu, R) = \chi P_0 \frac{c\tau}{2} AR^{-2}(\beta_m(\nu, R)(\beta_a(\nu, R))\exp\left[-2\int_0^R \alpha(\nu, R)dR\right] \quad (2)$$

where P_0 is the power of the laser radiation transmitted from the lidar location, c is the speed of light, τ is the laser pulse duration, A is the effective area of the lidar receiver optical system, χ is the transmittance of the receiver optics, β_M (ν,R) and β_A(ν,R) are the volume coefficients of molecular and aerosol backscattering, and α(ν,R) is the profile of the atmosphere extinction coefficient, which can be described as the sum of the coefficients of extinction due to absorption, scattering by aerosols, and atmospheric gas molecules:

$$\alpha(\nu, R) = \alpha_{ma}(\nu, R) + \alpha_{ms}(\nu, R) + \alpha_{aa}(\nu, R) + \alpha_{as}(\nu, R) \quad (3)$$

where α_{ms}(ν,R), α_{aa}(ν,R), and α_{as}(ν,R) are the extinction volume coefficient profiles due to molecular scattering, atmospheric aerosol absorption and scattering, respectively; and α_{ma}(ν,R) is the profile of the extinction volume coefficient due to molecular absorption.

3.2. IPDA

Based on the Integrated-Path Differential Absorption (IPDA) method [64], a signal is recorded from various topographic objects that is reflected or diffusely reflected (Figure 2).

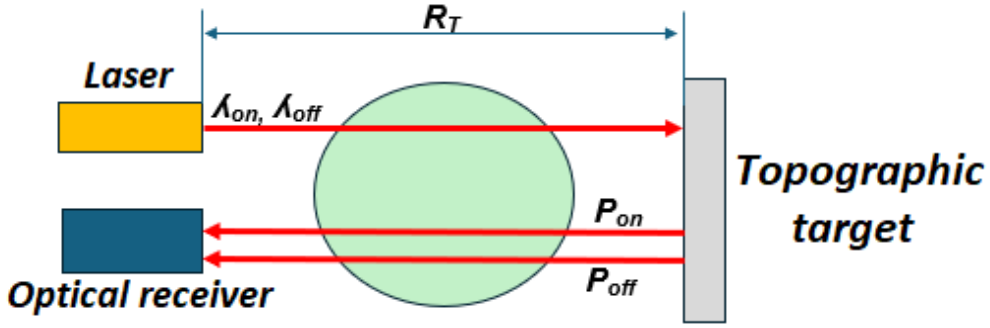


Figure 2. IPDA—Integrated-Path Differential Absorption.

The method is based on detecting backscattered signals reflected from various sources (topographic targets with different surface albedos). The IPDA lidar uses a laser beam scattered back from the surface ("topographic target") to measure the column content of a specific atmospheric residual gas between the lidar and the target. The topographic target is located *R* away from the laser source. The topographic target can be a land surface, sea surface, cloud tops, etc.

Figure 3 shows the basic operation of DIAL/IPDA lidars for aircraft and satellite greenhouse gas measurements.

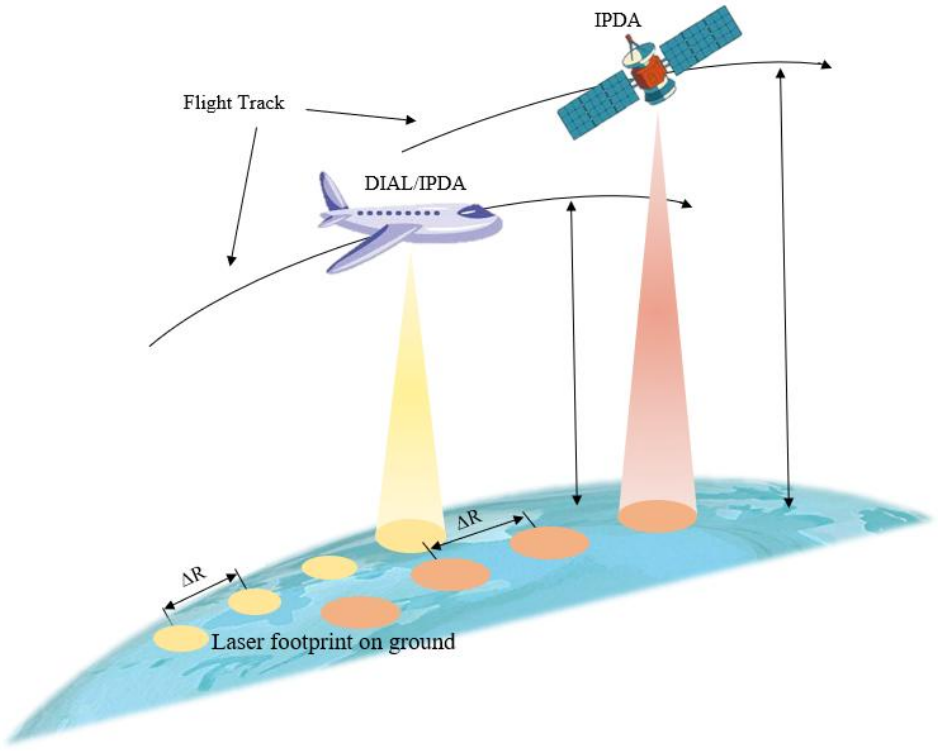


Figure 3. Schematic diagram of the DIAL/IPDA lidar for aircraft and satellite measurements.

In the case of a topographic target using the lidar, Equation (2) is modified somewhat to look like [65,66]:

$$P(\lambda_i, R_T) = \frac{E_0(\lambda_i)}{\Delta t_{eff}} D'(\lambda_i) \frac{d\rho(\Omega, \lambda_i)}{d\Omega R_T^2} exp[-2\int_{R_0}^{R_T} \alpha(\lambda_i, R) dR] \quad (4)$$

where, instead of the molecular and aerosol backscattering volume coefficients $\beta_M(\nu,R)$ and $\beta_A(\nu,R)$, the differential surface albedo $\frac{d\rho(\Omega,\lambda_i)}{d\Omega}$, characterizing the energy and angular distribution of the reflected optical signal, are used; and $\underline{\Omega}$ is the solid angle. Here, $E_0(\lambda_i)$ is the energy of the radiation per pulse at the wavelength λ_i, $D'(\lambda_i)$ is the instrumental function, and $\alpha(\lambda_i,R)$ is the profile of the atmosphere extinction coefficient. The parameter Δt_{eff}, which considers the time distribution of the reflected pulse, plays an important role when processing a signal reflected from a dense topographic target, as in Equation (4).

In the approximation of an ideal Lambert surface, a simplified expression of $\frac{d\rho(\Omega,\lambda_i)}{d\Omega} = \rho(\lambda_i)/\pi$ can be used, where $\rho(\lambda_i)$ is the topographic target albedo. In processing signals reflected from the dense topographic target, the parameter Δt_{eff} in Formula (4), accounting for the distribution of reflected pulse in time, starts playing a significant role. In the general case, this parameter depends on the pulse duration τ and the time of detector response $\Delta t_D = 1/(3\Delta B)$, where B is the electric signal transmission band of the receiving–amplifying system, and on the time of the pulse expansion during scattering on inhomogeneities of the topographic target surface. Gaussian distribution is conventionally used to analytically describe these effects, and the effective pulse length is determined on the base of the convolution theorem as a geometric sum of individual half-widths:

$$\Delta t_{eff} = \sqrt{\Delta t_L^2 + \Delta t_D^2 + \Delta t_T^2} \quad (5)$$

where Δt_L is the laser pulse length, and $\Delta t_T = 2\Delta h/c$, Δh is the topographic target effective height within the pulse spot (slope of the topographic target surface with respect to the normal of the laser beam incidence).

The equation directly yields the sought differential optical depth due to the concentration of measured gas [65,66]:

$$\Delta\tau_g = \frac{1}{2}\cdot\left(\ln\frac{P_{off}}{P_{on}} + \ln\frac{E_{on}}{E_{off}} + \ln\frac{\rho_{on}}{\rho_{off}} - 2\ln(\Delta\theta_A)\right) \quad (6)$$

where Θ_A is the differential optical depth due to aerosol extinction and absorption by foreign gases. Traditional path measurements are usually confined to the estimate of the average concentration of industrial pollutions or greenhouse gases:

$$\bar{n}_g = \frac{\Delta\tau_g}{R_T\cdot\Delta K} \quad (7)$$

where ΔK is the difference in on-line and of-line absorption coefficients of the studied gas. When the absorption coefficient varies with the altitude, this formula is unsuitable.

The IPDA method ensures high-sensitivity determination of the average concentrations of gas mixtures along optical sensing paths in directions corresponding to the azimuth of topographic targets. Similar to DIAL, laser pulses with on-line and off-line wavelengths are directed to the atmosphere. A sensitive photodetector traps the light backscattered from the topographic target. The averaged gas concentration on the sensing path R can be calculated using the ratio of backscattered signals.

4. Results of the Development of Onboard Lidar Systems for Sensing Greenhouse Gases in the Atmosphere

4.1. Onboard Lidars for CO_2 Sensing

Anthropogenic effects are considered the main cause of the sharp increase in carbon dioxide (CO_2) concentration in the atmosphere. Over the past 60 years, carbon dioxide concentration has increased by more than 100 ppm, and this rapid increase continues. Globally, this has led to glaciers melting, sea levels rising, and an increase in the average temperature at the planet's surface. Although CO_2 concentration in the atmosphere is widely acknowledged as the primary anthropogenic driver of climate change, its global balance remains uncertain. New methods, such as airborne lidar techniques, are needed to quantify the amount of CO_2 in the atmosphere so as to reduce uncertainty regarding carbon sources and sinks.

4.1.1. History of Development

One of the first works on the development of an onboard lidar system for measuring carbon dioxide concentrations was carried out in 2007 by authors from NASA Langley Research Center, Hampton, USA, as part of the medium-term space mission "Active Sensing of CO_2 Emissions over Nights, Days, and Seasons" (ASCENDS). In 2007, an onboard multifunctional fiber IPDA lidar was developed, operating in continuous wave (CW) mode with intensity modulation in the CO_2 absorption band at a wavelength of 1.57 μm [67–70].

In 2011, this lidar system was installed on a DC-8 aircraft for in situ measurements of atmospheric CO_2 profiles, which were used to derive the expected *CO_2* column values, and when compared to the lidar measurements over desert and vegetated surfaces, the lidar measurements were found to agree with the in situ-derived CO_2 columns to within an average of 0.17% or ~0.65 ppmv, with a standard deviation of 0.44% or ~1.7 ppmv [71,72].

As part of the same ASCENDS mission, another team from NASA's Goddard Space Flight Center developed an onboard CO_2 lidar operating at a wavelength of 1572 nm. This lidar was developed using a fiber-optic laser transmitter and photon counter, and conducted CO_2 absorption measurements during flight in December 2008.

The results showed the shape of the CO_2 absorption line and lidar signals, which corresponded to the expected changes with changes in the aircraft's altitude from 1.5 to 7.1 km and were in good agreement with the estimates of atmospheric CO_2 concentration based on nearly simultaneous contact measurements from the aircraft [73].

Using the coherent detection method, a 2.05 μm continuous laser absorption spectrometer was used to measure CO_2 concentrations in the atmospheric column from an airplane [74,75].

4.1.2. CO_2 Lidar Developments in Recent Years

We will consider the main developments in onboard lidar systems for CO_2 monitoring presented by the global scientific community in recent years.

Researchers from the DLR Institute of Atmospheric Physics, Germany, described the development of an onboard IPDA lidar system for measuring the vertical profiles of carbon dioxide and methane [76]. This lidar system is located in the German research aircraft laboratory HALO (High Altitude and Long Range Research Aircraft). Based on an optical parametric oscillator (OPO), the lidar system operates at wavelengths of 1572.02 nm (for CO_2 sensing) and 1645 nm (for methane sensing). The pulse energy is 10 mJ, and the pulse duration is ~20 ns. The receiving system consists of two telescopes at every wavelength, with InGaAs avalanche photodiodes (APDs) used as receivers. The first flights with the onboard lidar for measuring CO_2 and CH_4 were successfully completed in April–May 2015. A HALO laboratory aircraft and two Cessna aircraft participated in a CoMet expedition in 2018 that simultaneously measured CO_2 and CH_4 by lidar, passive remote sensing, and in situ measurements [77].

Later, after being upgraded for use on board the HALO aircraft (Gulfstream 550), this lidar system was named CHARM-F [78]. CHARM-F is primarily focused on remotely monitoring CO_2 and CH_4 in support of global satellite observations through the use of the lidar as an onboard demonstrator for future space missions (such as the MERLIN [79] and A-SCOPE [80] missions). The CHARM-F lidar is designed to simultaneously measure column-integrated CO_2 and CH_4 concentrations beneath the aircraft. The second goal of the CHARM-F project is to demonstrate the ability to measure powerful point sources of pollution. Measurements conducted near a large power plant demonstrate the possibility of studying CO_2 plumes with high spatial resolution and estimating the source's emission rate [78,79]. The CHARM-F lidar system consists of a transmitting part containing two lasers, a receiving optical system, and two aircraft racks that contain the laser's electronics and cooling system. For each gas being studied, there is a large telescope (200 mm) with a PIN photodiode as a detector and a small telescope (60 mm) with an APD. The laser radiation is generated by an OPO, which is pumped by a Nd:YAG laser. A 36 m long multi-pass cuvette filled with CO_2 and CH_4 is used for absolute wavelength calibration and stabilization of seed lasers. Double pulses with a 500-microsecond interval provide an almost complete overlap of laser spots on the ground on-line and off-line [78,79]. The CHARM-F lidar was flight-tested using the HALO aircraft in the spring of 2015. As part of the flight campaign, a second instrument was installed on board: the cavity ring down spectroscopy (CRDS) spectrometer. This allowed for contact measurements of CO_2, CH_4, CO, and H_2O. Comparison with the vertical profile of CO_2 (the concentration, which fluctuates around 403 ppm), obtained using both the CHARM-F lidar and the CRDS gas analyzer during several descents and ascents of the aircraft from 200 m to 9 km, indicates some distance-dependent deviations

in the concentration values in the atmospheric column. On May 13, 2015, the HALO flight path included a pass over coal-fired power plants in East Germany. A significant increase in CO_2 concentration was observed near the Jänschwalde power plant [78].

The authors from the Japan Aerospace Exploration Agency (JAXA), Tsukuba, Japan, reported simultaneous measurements of the column-averaged CO_2 concentration in dry air (XCO_2) and the range to the target using an onboard differential laser absorption spectrometer (LAS lidar) with amplitude modulation at a wavelength of 1.57 μm [81]. In the first step, the authors created a ground-based prototype of the LAS lidar system [82,83]. Subsequently, the LAS lidar was installed on a Beechcraft King Air aircraft. Each flight lasted approximately 4 h, including spiral and level flights. The aircraft measurements were conducted using the spiral flight method over the Tsukuba (0.5–2 km) and Koganei (0.5–3 km) areas. To verify the LAS lidar system measurements, atmospheric CO_2 was sampled at altitudes ranging from 0.5 km to 7 km via sampling flasks and instruments for in situ CO_2 measurement. The on-line and off-line emission sources were polarization-maintained diode lasers connected to optical fibers. A gas cell filled with CO_2 at 0.1 atm was used instead of a reference cavity. The transmitted beam diameter was 60 mm, and the full angular divergence was 0.12 mrad. The total transmitted power at the end of the fiber was 1.2 W. A receiving telescope with a field of view of 0.2 mrad and a lens diameter of 110 mm was used to collect scattered signals from the ground surface. The column concentrations of CO_2 measured by the LAS lidar system varied between 370 and 410 ppm on various days [81]. According to the LAS lidar system, the XCO_2 measured by LAS and the XCO_2 calculated from in situ measurements had a high correlation coefficient of 0.987. Airborne in situ CO_2 measurements were conducted using a module consisting of a commercial CO_2 analyzer (LI-COR, Inc., Type: LI-840) modified for airborne operations. The average difference in XCO_2 between LAS and CO_2 analyzer data was less than 1.5 ppm for all spiral measurements. In urban areas, where the atmospheric boundary layer contains high levels of CO_2 and aerosols during winter, the difference between the XCO_2 LAS and XCO_2 in situ values was a negative offset of 1.5 ppm, and the XCO_2 LAS values matched the XCO_2 in situ values with a measurement accuracy of 2.4 ppm.

The work by the authors from NASA Goddard Space Flight Center, Greenbelt, USA, presents the results of measurements performed with the advanced CO_2 Sounder lidar during the 2017 ASCENDS/ABoVE air campaign [84,85]. The changes made to the 2011 version of the CO_2 Sounder lidar [86,87] included the use of a fast wavelength switching laser with step-by-step synchronization in the transmitter and a more sensitive APD HgCdTe detector. The lidar uses a tunable diode laser with a modulator for pulse generation and a series of laser amplifiers. The NASA DC-8 aircraft conducted flights over various types of topographic surfaces at altitudes ranging from 3 to 12 km in the continental USA area. The results were compared with the XCO_2 values calculated by an in situ onboard sensor during the aircraft's spiral lowering. The measurements performed using the onboard lidar in 2016 showed an accuracy of approximately 0.7 ppm. This is approximately eight times better than similar measurements conducted in 2011. The results of both campaigns demonstrated that the average XCO_2 values obtained using the lidar consistently matched the values obtained from the in situ sensor. This was achieved with an accuracy of up to 1 ppm.

In Hampton, USA, NASA's Langley Research Center (LaRC) developed an onboard two-pulse IPDA lidar system to measure the total integrated CO_2 content in the atmospheric column [88–90]. The lidar uses a CO_2 R30 absorption line centered on 2050.9669 nm. The transmitter provides a total maximum output energy of 80 mJ at a wavelength of 2 μm. The pump pulse repetition rate was 50 Hz, with a 200 μs interval between the two pulses. The off-line wavelength was set to 2051.1905 nm, 15.9 GHz away from the

R30 line center. The transmitting pulse energies were approximately 17.5 and 6.0 mJ for the on-line and off-line pulses, respectively. The flight campaign took place in late 2019 and included four flights, with a total duration of 15 h aboard a NASA B-200 aircraft [47]. The LaRC IPDA lidar was tested over the ocean to determine the weighted average volume ratio of CO_2 in the dry air column (XCO_2) at an altitude of 4.5 km. The XCO_2 measurement gave a result of 404.43 ± 1.23 ppm when averaged over 10 s. This is compared to 405.49 ppm obtained using forecasting models [88].

Researchers from the Shanghai Institute of Optics and Fine Mechanics, Chinese Academy of Sciences, report the development of an onboard dual-pulse IPDA lidar system with a wavelength of 1.57 μm for measuring CO_2 concentration [91]. This IPDA lidar is a scaling-up prototype of China's planned space-based IPDA lidar system [92]. Flight experiments using the IPDA lidar system were conducted at an altitude of approximately 7 km in an oceanic region. The flight path took place through oceanic, residential, and mountainous areas, with an average XCO_2 value of 419.35, 429.29, and 422.52 ppm, respectively. The gradient in residential and marine areas was 9.94 ppm, while the gradient in urban and mountainous areas was 6.77 ppm. The correlation coefficient between the XCO_2 trends obtained using the IPDA lidar system and the volumetric CO_2 concentration in dry air measured by an in situ instrument was 92%. In an area 30 km away from the coast, which is largely unaffected by urban areas, the average XCO_2 value obtained using the IPDA lidar system was 414.69 ppm. This was with a standard deviation of 1.02 ppm. CO_2 concentrations measured locally by the same instrument during the same period were offset by 1.30 ppm [91].

4.1.3. Brief Analysis

Table 2 summarizes the main characteristics of the abovementioned airborne IPDA lidar systems for CO_2 sensing [76–92].

Table 2. Airborne differential absorption (IPDA) lidars for CO_2 sensing *.

Lidar System	Laser Source	Wavelength, nm	Laser Parameters	Telescope, m	Photodetector	Ranges, km	Reference
CHARM-F, DLR Institute of Atmospheric Physics, Germany	OPO Nd:YAG	1572.02	E = 10 mJ; Δω = 50 MHz; τ = 20 ns; f = 50 Hz	Cassegrain 2 × 0.2 2 × 0.06	APD PIN photodiodes	From 0.2 to 8	[78,79]
LAS, Japan Aerospace Exploration Agency, Japan	Cw fiber-coupled diode lasers	1572.992 1573.193	W = 1.2 W; Δω = 0.8 MHz; Θ = 0.12 mrad;	Cassegrain 0.11	PIN InGaAsdetector	From 0.5 to 7	[81–83]
CO_2 Sounder Lidar, NASA Goddard Space Flight Center, USA	DFB laser diode	1572.335	E = 50 μJ; τ = 1 μs; f = 10 kHz; Θ = 430 μrad; Δν = 0.001 cm^{-1}	Cassegrain 0.2	DRS HgCdTeAPD	From 3 to 12	[84–87]
LaRC IPDA NASA Langley Research Center, USA	Ho:Tm:YLF laser	2050.9669/2051.1905	E = 17.5/6 mJ; τ = 200 μs; f = 50 Hz	Newtonian 0.4	InGaAs Detector HgCdTeAPD	From 1.6 to 8	[88–90]
IPDA LIDAR Shanghai Institute of Optics and Fine Mech., China	DFB laser diode	1572.024 1572.085	E = 6/3 mJ; τ = 17 ns; f = 30 Hz; Δω = 30 MHz; Θ = 0.62 mrad	Cassegrain 0.15	InGaAs APD photodiode IAG350H1D	From 2 to 7	[91,92]

* E—energy in radiation pulse; W—laser power; Δν, Δλ, Δω—radiation line width (cm^{-1}, pm, MHz, respectively); τ—radiation pulse duration; f—pulse repetition frequency; Θ—laser radiation divergence.

From Table 2 and the above description of the developments of airborne IPDA lidar systems for CO_2 sensing, the following conclusions can be drawn:

(1) The CO_2 lidars described above operate either in a fairly strong carbon dioxide absorption band of 2 μm, or in a weaker absorption band of 1.57 μm;

(2) For CO_2 sensing using airborne mobile lidars, DFB lasers with lower energy are most often used, which allows for the generation of wavelengths in the near-IR range in the region of a CO_2 absorption band of about 1.57 μm. Less often, Ho:Tm:YLF or OPO Nd:YAG lasers are used to operate in the region of the carbon dioxide absorption band of about 2 μm;

(3) The receiving optics in airborne carbon dioxide lidars are represented by Newtonian or Cassegrain telescopes with a diameter of 0.15–0.4 m;

(4) Airborne carbon dioxide lidars use various semiconductor photodiodes as receivers, with peak sensitivity in the region of the probing laser radiation;

(5) CO_2 sensing ranges range from 0.2 to 12 km depending on the aircraft's flight altitude.

Thus, the onboard IPDA lidar systems described in this section are capable of large-scale mapping and quantification of the integrated carbon dioxide content in the atmosphere of various climate zones.

4.2. Onboard Lidars for H_2O Sensing

Water vapor (H_2O) is the most active greenhouse gas. The increase in atmospheric temperature due to other greenhouse gases causes an increased concentration of water vapor in the air. This accelerates the greenhouse effect and speeds up the increase in temperature, contributing to even more evaporation. Water vapor contributes most to the natural greenhouse effect, but direct anthropogenic emissions have a minimal impact on climate change. Lidar as an active tool for remote laser sensing, especially when using an aircraft carrier, measures the concentration of water vapor on a significant spatial scale. This is carried out with high temporal resolution and accuracy.

4.2.1. History of Development

One of the first works on developing an onboard DIAL lidar system for remote measurements of atmospheric water vapor concentrations was by NASA Langley Research Center, Hampton, USA, in 1994 [93]. A solid-state alexandrite laser with a line width of 1 pm was used as a transmitter. In the receiving system, photomultipliers were replaced by solid-state APD detectors, which provide a signal-to-noise ratio increase of 1.5–2.5 times.

Flight tests of the system were conducted on a NASA Electra aircraft. Comparative measurements were performed utilizing hygrometers and radiosonics. The H_2O distributions measured by the DIAL system differ by less than 10% from profiles determined using in-situ probes. In 1996, the same team reported on the development of a differential lidar (DIAL) for measuring water vapor in the troposphere as part of the Lidar Atmospheric Sensing Experiment (LASE).

The LASE lidar transmitter uses a Ti:Sapphire laser with a pulse width of 30 ns and a pulse energy of 150 mJ for operation on board the NASA/Ames ER-2 aircraft flying at altitudes of 16 to 21 km [94].

As part of the unique IHOP 2002 project [95], four onboard aircraft lidars (LASE from NASA Langley based on the NASA DC-8 aircraft [96], DLR DIAL-DLR Falcon air-

craft [97], Leandre II from the CNRS-NRL P-3 aircraft [98], and CODI from the NOAA/ETL–ARM CART CF aircraft [99]) were used simultaneously to measure water vapor profiles.

Also, Langley Research Center, Hampton, USA, developed the DIAL lidar system to measure water vapor on the Altair UAV [100]. The design included a microchip laser transmitter based on a Nd:YAG laser and a diode laser for narrowing the absorption line and locking the Nd:YAG laser to the 946.0003 nm water vapor absorption line.

4.2.2. H_2O Lidar Developments in Recent Years

In this section, we will analyze the main developments in onboard lidar systems for H_2O monitoring presented by the global scientific community in recent years.

An onboard DIAL lidar system for measuring vertical water vapor profiles [101,102] has been developed by researchers from the DLR Institute of Atmospheric Physics, Germany. In [102], the results of joint observations are presented, carried out using a DIAL system and a Doppler wind lidar, both installed on the same aircraft. Water vapor profiles obtained by DLR DIAL are highly accurate in both the troposphere and the lower stratosphere, where water vapor concentrations can vary by up to four orders of magnitude. DLR DIAL has two laser transmitters. Each is based on an OPO operating at the second harmonic of a single-mode Nd:YAG laser with diode pumping and Q-switched mode, a pulse repetition rate of 100 Hz, and an average output pulse energy of 40 mJ [101,102].

NASA Langley Research Center (LaRC) in Hampton, USA, has developed an onboard three-pulse IPDA lidar system operating in the spectrum range of 2 μm for simultaneous and independent measurements of the integral content of H_2O and CO_2 [103,104]. This system uses CO_2 at a wavelength of 2 μm, which is a development of the IPDA two-pulse lidar system [88–90]. In the LaRC IPDA lidar, the IPDA three-pulse lidar transmitter generates three consecutive laser pulses for each pump pulse. The CO_2 sensing wavelengths are selected near absorption line R30 so that both lines have similar H_2O absorption, which minimizes interference from water vapor during CO_2 measurement. Similarly, H_2O wavelengths are selected near the closest peak of water vapor absorption to minimize interference from carbon dioxide when measuring H_2O. Moreover, CO_2 measurements on-line and H_2O measurements off-line use the same wavelength, allowing both molecules to be measured simultaneously with three pulses rather than four. The laser is pumped through AlGaAs laser diodes with a wavelength of 792 nm. The repetition rate of pump pulses is 50 Hz, and the time between pulses is 150–200 microseconds. Setting the energy of successive pulses to 13.3, 10.4, and 11.4 mJ results in pulse durations of 43.7, 55.6, and 54.3 ns, respectively. During the onboard aircraft test, a PICARRO gas analyzer was used for in situ monitoring of CO_2 and H_2O. Lidar performed nine flights over the ocean off Cape May, New Jersey, on board a NASA B-200 IPDA lidar aircraft. The B-200 then flew over land northeast of Baltimore, Maryland, at an altitude of 5 km to investigate urban emissions and over the Roxboro Power plant (Semora, North Carolina) at different altitudes during the day and at night to identify emissions. Statistical analysis of simultaneous and independent measurements of CO_2 and H_2O using a three-pulse 2 μm IPDA lidar shows 500-pulse average concentrations of CO_2 425.9 ± 6.0 ppm and H_2O 5353.2 ± 496.6 ppm [103,104].

In 2019, another team of authors from NASA Langley Research Center (LaRC), Hampton, USA, as part of the HALO (High Altitude Lidar Observatory) project [105], developed an onboard aircraft DIAL lidar method for measuring water vapor concentration profiles [106,107]. Due to its compact design using a single laser transmitter at all wavelengths, the HALO DIAL lidar can be installed on most research aircraft. This includes NASA's ER-2 aircraft, designed for autonomous operation at high altitudes. The

HALO DIAL lidar uses four wavelengths near 935 nm to achieve DIAL sensitivity over a wide dynamic range. In the lower few hundred meters of the atmosphere, water vapor is measured with a strong surface reflection signal. Five flights of the HALO DIAL lidar covered the tropics and mid-latitudes under a wide range of atmospheric conditions. Comparison with in situ measurements of water vapor content on board the aircraft did not reveal a significant shift. The measurements of water vapor obtained using the AIRS and IASI satellites coincided very well with the results of the HALO DIAL. These were achieved with a correlation coefficient of 0.96 over the ocean [106,107].

An international team of European authors within the framework of the EU H2020 LEMON project (Lidar Emitter and Multispecies greenhouse gases Observation iNstrument) [108] presented the development of an onboard LEMON DIAL lidar for greenhouse gas monitoring. It was designed to study H_2O and its isotope HDO at a wavelength of 1982 nm, CO_2 at a wavelength of 2051 nm, and CH_4 at a wavelength of 2290 nm using a DIAL lidar. The lidar IR emitter uses a combination of two optical parametric generators with two Nested Cavity OPOs (NesCOPOs) and one optical parametric amplification (OPA) line to generate high-energy pulses. Parametric cascades are pumped by an Nd:YAG laser providing nanosecond double pulses with an energy of 200 mJ at a frequency of 75 Hz with an output energy of 40–50 mJ [109].

4.2.3. Brief Analysis

Table 3 summarizes the main characteristics of the above-mentioned airborne DIAL/IPDA lidar systems for H_2O sensing [101–109].

From Table 3 and the above description of the developments of airborne DIAL/IPDA lidar systems for H_2O sensing, the following conclusions can be drawn:

(1) The H_2O lidars described above operate either in a fairly strong water vapor absorption band of 2 μm, or in a weaker absorption band of 935 nm;

(2) For H_2O sensing using airborne mobile lidars, OPO Nd:YAG lasers are used, which allows for the generation of wavelengths in the near-IR range in the region of a water vapor absorption band of about 935 nm. Less often, Ho:Tm:YLF lasers are used to operate in the region of the water vapor absorption band of about 2 μm;

(3) The receiving optics in airborne water vapor lidars are represented by Newtonian or Cassegrain telescopes with a diameter of 0.35–0.48 m;

(4) Airborne water vapor lidars use various semiconductor photodiodes as receivers, with peak sensitivity in the region of the probing laser radiation;

(5) Water vapor sensing ranges range from 0.2 to 10 km depending on the aircraft's flight altitude.

Table 3. Airborne differential absorption lidars for H_2O sensing *.

Lidar System	Laser Source	Wavelength, nm	Laser Parameters	Telescope, m	Photodetector	Ranges, km	Reference
DLR DIAL, DLR Institute of Atmospheric Physics, Germany	OPO Nd:YAG	935.6846 935.5612	E = 40 mJ; Δω = 0.14 GHz; τ = 20 ns; f = 100 Hz	Cassegrain 0.48	APD PIN photodiodes	From 0.5 to 8, resolution 15 m	[101,102]
LaRC IPDA, NASA Langley Research Center, USA	Ho:Tm:YLF laser	2050.967 2051.059 2050.509	E = 13.3/10.4/11.4 mJ; τ = 43.7/55.6/54.3 ns; f = 50 Hz	Newtonian 0.4	InGaAs Detector HgCdTeAPD	From 2.5 to 7.7	[103,104]

HALO DIAL, NASA Langley Research Center, USA	OPO Nd:YAG	935.5	E = 1.50 mJ; τ = 20 ns; f = 1 kHz	Cassegrain 0.4	APD photodiodes	From 0.2 to 10, resolution 250–585 m	[105–107]
LEMON DIAL ONERA/LATMOS/LSCE, France; Royal Inst. Tech., Sweden; Space Tech, Germany; Univ. Bergen, Norway	NescOPO Nd:YAG	1982	E = 50 mJ; τ = 10 ns; f = 75 Hz;	Newtonian 0.35	InGaAs PIN photodiode		[108,109]

* E—energy in radiation pulse; Δν, Δλ, Δω—radiation line width (cm^{-1}, pm, MHz, respectively); τ—radiation pulse duration; f—pulse repetition frequency; Θ—laser radiation divergence.

4.3. Onboard Lidars for CH_4 Sensing

Methane is one of the most significant organic substances in the atmosphere. Monitoring its concentration levels and distribution profiles in the atmosphere is relevant due to the strong influence of this gas component on Earth's climate [110,111]. The methane molecule consists of one carbon atom and four hydrogen atoms. CH_4 is one of the gases most frequently measured using a differential technique [18,19] at various concentrations ranging from ppb to ppm. Methane is also a powerful greenhouse gas with a high potential for global warming, which contributes to climate change. The concentration of methane in the atmosphere increased sharply from about 0.8 ppm (early 1900s) to 1.8–2 ppm (2016–2025) [112].

4.3.1. History of Development

One of the first works on the creation of an airborne mobile lidar system for sensing methane and other gas components was developed by authors at LaSen and the Air Force Research Laboratory, USA. Initially, the Lidar I ground-based mobile lidar system was created. This system, based on test measurements conducted during ground monitoring of leaks in gas pipeline systems, was upgraded to the onboard Lidar II version [113]. This lidar weighs about 30 kg and occupies a volume of 0.08 m^3. It can be used both on the ground and in measurement mode from a helicopter. Helicopter speed is limited to 30 km/h due to the pulse repetition rate of 10 Hz and averaging. Ground tests measured methane levels from 5 to 100 ppm · m [113].

4.3.2. CH_4 Lidar Developments in Recent Years

The article [114] contains measurements of total methane content in the atmosphere in the altitude range of 3–11 km by NASA Goddard Space Flight Center, Greenbelt, USA. These were carried out using an onboard pulsed IPDA lidar system. The operating wavelength was 1651 nm (near the one of the strongest methane absorption lines), obtained by converting Nd:YAG pumping laser radiation (1064 nm) due to parametric light generation. During the operation of this system, discrete tuning was performed for 20 wavelengths of 1651 nm (including on-line and off-line methane absorption wavelengths). The main characteristics of the transmitting part of the system are: pulse duration 3 ns, pulse energy 30 μJ, divergence 300 μrad. The main characteristics of the receiving part of the system are: diameter of the receiving aperture of the telescope of 200 mm, and field of view of the telescope of 300 μrad. At the receiving part, a photon-counting photomultiplier tube (PMT) is used. During the IPDA flight tests, the system was placed on board the NASA's DC-8 aircraft [114]. The flights were conducted in early August 2011 in the Central Valley, where there are possible sources of methane (livestock farms, oil fields and natural gas storage facilities). Each flight lasted about 2.5 h and consisted of several altitude measurements segments. 3; 4.8; 6.24; 7.9; 9.5; 11.1 km.

A Picarro laser CRDS gas analyzer was used to calibrate lidar measurements by in situ measurement of methane [114].

The first NASA IPDA experiment prompted the system upgrade [115]. The upgraded OPA/OPO IPDA system generated informative methane sensing wavelengths (central wavelength 1650.958 nm, with discrete tuning to 20 wavelengths near the central wavelength) with pulse energies of 25–30 μJ and 250 μJ, respectively. A highly sensitive avalanche photodetector was used in the receiving part of the system. At the end of September 2015, the IPDA system was installed in NASA's DC-8 airborne laboratory. The first results showed the possibility of measuring methane from an airplane and identified those points that required solutions for more accurate measurements in the future. Three flights were conducted in the western USA area in late September and early October 2015. Each flight lasted about 4 h and included several test segments at altitudes of 2 to 13 km. This depended on the topography of the terrain, the reflectivity of the Earth (including the ocean), and atmospheric conditions.

The authors from the DLR Institute of Atmospheric Physics, Germany, reported on the development of an onboard IPDA system for measuring the vertical profile of methane and carbon dioxide. This system was placed in the German research aircraft laboratory HALO (High Altitude and Long Range Research Aircraft) [116]. Later, this lidar system received the abbreviation CHARM-F (CO_2 and CH_4 Remote Monitoring—Flugzeug), which was mentioned in [78,79]. The CHARM-F lidar system uses two OPOs and operates at wavelengths near 1571 nm (for CO_2 sensing) and 1645 nm (for methane sensing). The pulse energy is 10 mJ, and the pulse duration is ~20 ns. The receiving part of the system consists of two telescopes for each lidar sounding channel. InGaAs APDs are used as receivers. In April–May 2015, the first flights were successfully completed using the onboard IPDA system for measuring CO_2 and CH_4.

The CoMet expedition in 2018 conducted simultaneous measurements of CO_2 and CH_4 using the onboard IPDA system, passive remote sensing, and in situ measurements. This was carried out in coordination with the HALO laboratory aircraft and two Cessna aircraft [77]. The CoMet 1.0 mission in 2018 continued the 2017 campaign with research flights focused on measuring greenhouse gases (CO_2 and CH_4) over Europe. In particular, the flights took place over one of the most powerful sources of methane emissions in the European Union, the Upper Silesian Coal Basin (southern Poland). The mission assessed methane emissions from coal mining ventilation shafts in the Upper Silesian Coal Basin. The results of these studies are described in detail [117–119]. Researchers used global–regional numerical climate models to separate local emissions from coal mines from background methane fluctuations when processing and analyzing flight experiments. CoMet's goal is to combine a set of the best active (laser-location, lidar) and passive remote instruments available at the time of research, as well as in situ meters to obtain greenhouse gas data on a regional scale.

European and American researchers conducted simultaneous measurements of CH_4 content and optical properties of aerosol during NASA's Atmospheric Carbon and Transportation-America (ACT-America) 2019 air campaign [120,121].

At the same time, the HALO/CHARM-F lidar [122] was an upgraded version of the previously developed HALO lidar [105–107] specifically for the 2019 ACT-America campaign.

In August 2021, an international campaign called MAGIC-2021 (Monitoring of Atmospheric composition and Greenhouse gases through multi-Instruments Campaigns) was held in Scandinavia to study regional emissions and transport of CH_4 and CO_2 [122]. During this campaign, an aerial experiment was conducted to perform simultaneous measurements of CO_2/CH_4 using the CHARM-F IPDA lidar, as well as range-resolved wind profiles using a coherent Doppler lidar [123].

Bridger Photonics researchers reported on the development of a LiDAR gas mapping system (GML) for monitoring methane emissions and controlling emissions levels from oil and gas systems [124,125].

The GML lidar system integrates spatially scanned and combined topographic and trajectory-integrated LiDAR methane concentration measurements with navigation data and aerial photography.

This combination enables episodic detection, localization, quantification of emission rates, and identification of sources of methane plume emissions in the scanned infrastructure.

Aerial deployment provides fast and efficient coverage of large and dispersed infrastructure.

Highly sensitive LiDAR measurements can detect more than 90% of methane emissions in the studied areas. The high spatial resolution of LiDAR scanning provides identification of the geographical location of emission sources, usually with an accuracy of up to 2 m [124,125].

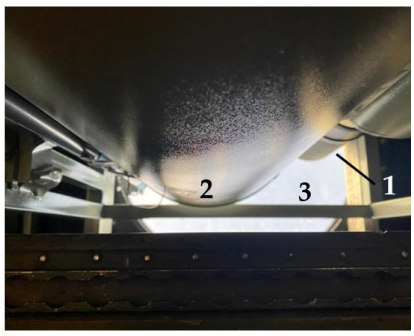
As a prototype for an airborne lidar system designed to detect methane, a ground-based mobile IPDA lidar [126–129] was developed at the V.E. Zuev Institute of Atmospheric Optics of the Siberian Branch of the Russian Academy of Sciences (IAO SB RAS). This system incorporates a laser based on an optical parametric oscillator (OPO) manufactured by the company SOLAR LS [130].

The prototype is of particular interest because it was tested in the Russian sector of the Arctic—a region that is otherwise difficult for the broader scientific community to access.

The exterior view of the IAO SB RAS lidar [131] installed on board the TU-134 Optik laboratory aircraft is shown in Figure 4.



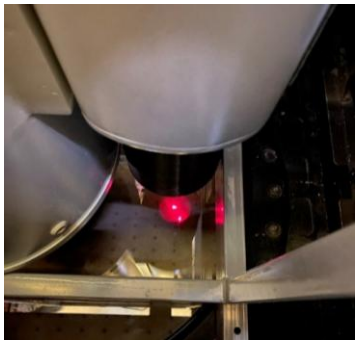
(**a**)



(**b**)



(**c**)



(**d**)

Figure 4. Exterior view of the methane lidar mounted on board the TU-134 Optik laboratory aircraft (**a**); top view (**b**) of the transmitting aperture of the transmitter with an additional tube (1), receiving aperture (2), aircraft hatch (3); bottom view (**c**) of the receiving and transmitting aperture of the lidar; and photograph (**d**) of the outputs of laser beams at on-line and off-line wavelengths after the collimator (the red alignment laser is aligned coaxially with informative on- and off-line IR radiation).

An IAO SB RAS flight expedition was conducted on a TU-134 Optik laboratory aircraft from 6 to 11 September 2022, on the route Novosibirsk–Salekhard–Kara Sea–Salekhard–Tomsk.

For the first time, lidar for measuring methane was installed on board this laboratory aircraft. Experimental measurements were carried out (the probe trajectory was vertically down through the hatch of the aircraft) and a large amount of experimental data was accumulated on lidar methane sensing at various altitudes of the aircraft**.**

The aircraft was also equipped with a Picarro gas analyzer. This made it possible to compare lidar methane concentration measurements with in situ measurements.

Detailed results of the lidar prototype development and flight expedition are presented in the article [131].

In general, the flight expedition and the first experimental measurements showed satisfactory operation of the created aircraft lidar configuration for sensing CH_4 in the atmosphere.

4.3.3. Brief Analysis

Table 4 summarizes the main characteristics of the above-mentioned airborne DIAL/IPDA lidar systems for CH_4 sensing [78,79,114,115,122,131].

Table 4. Airborne differential absorption lidars for CH_4 sensing *.

Lidar System	Laser Source	Wavelength, nm	Laser Parameters	Telescope, m	Photodetector	Ranges, km	Reference
NASA IPDA, NASA Goddard Space Flight Center, USA	OPA/OPO Nd:YAG	1650.958	E = 30/250 μJ; Δω = 300 MHz; Θ = 150 μrad; f = 5 kHz	Newtonian 0.2	HgCdTe e-ADP	From 0.5 to 14	[114,115]
CHARM-F, DLR Institute of Atmospheric Physics, Germany	OPO Nd:YAG	1645.00	E = 10 mJ; Δω = 50 MHz; τ = 15 ns; f = 50 Hz	Cassegrain 2 × 0.2 2 × 0.06	APD PIN photodiodes	From 0.2 to 8	[78,79]
HALO DIAL/IPDA,	OPO Nd:YAG	1645.5518 1645.3724	E = 2.5 mJ; τ = 15 ns;	Cassegrain 0.4	APD photodiodes	From 0.2 to 10, Δh	[122]

NASA Langley Research Center, USA			f = 500 Hz Θ = 0.4 mrad;			15 m	
IAO IPDA, IAO SB RAS, Tomsk, Russia	OPO Nd:YAG	3428.7083430.532 3428.180 3430.532	E = 4.5 mJ; τ = 10 ns; Δν = 1.5 cm^{-1}; f = 20 Hz;	Cassegrain 0.3	VIGO photodiode	From 0.2 to 11	[131]

* E—energy in radiation pulse; Δν, Δλ, Δω—radiation line width (cm^{-1}, pm, MHz, respectively); τ—radiation pulse duration; f—pulse repetition frequency; Θ—laser radiation divergence.

From Table 4 and the above description of the developments of airborne DIAL/IPDA lidar systems for CH_4 sensing, the following conclusions can be drawn:

(1) The CH_4 lidars described above operate either in a fairly strong water vapor absorption band of 3 μm, or in a weaker absorption band of 1.65 μm;

(2) For CH_4 sensing using airborne mobile lidars, OPO Nd:YAG lasers are used, which allows for the generation of wavelengths of the near-IR range in the region of a water vapor absorption band of about 1.65 μm nm. Less often, OPO Nd:YAG lasers are used to operate in the region of the water vapor absorption band of about 3 μm;

(3) The receiving optics in airborne water vapor lidars are represented by Newtonian or Cassegrain telescopes with a diameter of 0.2–0.4 m;

(4) Airborne methane lidars use various semiconductor photodiodes as receivers, with peak sensitivity in the region of the probing laser radiation;

(5) Methane sensing ranges range from 0.2 to 11 km depending on the aircraft's flight altitude.

4.4. Onboard Lidars for O_3 Sensing

An important step toward developing research ozone lidars has been the transfer and adaptation of lidar systems to mobile onboard platforms: vessels [132,133] and aircrafts [134–139], expanding the capability range of lidar groups; in particular, most of the difficulties in expedition campaigns have been addressed, and it has been possible to carry out research in different territories by united groups of mobile lidar systems.

4.4.1. History of Development

One of the first mobile lidar systems was ozone lidar (Langley Research Center airborne ozone lidar) [134], created in 1998. It was mounted on board aircraft (preliminary field tests were carried out with a ground-based version) and uses a dye laser (Lasers Continuum Model ND 6000 flashlamp-pumped Nd:YAG, Model 9030 dye lasers) pumped by Nd:YAG to generate wavelengths of 290/300 nm with 30 mJ pulse energy and 30 Hz frequency. The lidar system comprises two 35.5 cm diameter mirror Cassegrain telescopes operating to the zenith and to the nadir. The covered altitude range is from the surface layer to 15 km.

The ozone onboard DIAL lidar for aircraft is the Tunable Optical Profiler for Aerosol and oZone lidar (TOPAZ), which was designed and built in 2006 at the NOAA Chemical Sciences Laboratory [135]. TOPAZ incorporates state-of-the-art technologies to make it compact and lightweight, and have low power consumption. These features have allowed for flexibility in its application to numerous air quality field studies, both airborne and ground-based.

TOPAZ was originally configured and deployed on the NOAA Twin Otter aircraft to participate in air quality studies, where it provided wide-area mapping of ozone and aerosol distributions and transport near urban sources [136]. The first example of this application was the Texas Air Quality Study (TexAQS) in 2006 [135]. After several years

of airborne operation, TOPAZ was reconfigured for deployment in a box truck (and, more recently, a trailer) for ground-based operation [135].

4.4.2. O_3 Lidar Developments in Recent Years

The modern TOPAZ mobile system [137] is an onboard three-wave DIAL lidar system based on an Nd:YLF pump laser for Ce:LiCAF at 283–310 nm sensing wavelengths, with an output pulse energy of 0.1 mJ and a repetition frequency of 1 kHz. The lidar includes a telescope (according to the Newton scheme) with a receiving mirror diameter of 0.4 m. TOPAZ allows one to obtain profiles of ozone and aerosols from approximately 400 m under the aircraft to the surface layer (flights are usually performed at altitudes 3 to 5 km above sea level). The spatial resolution of the lidar signals corresponds to 90 m. TOPAZ data is recorded in segments of 10 s. There is an adaptation of the TOPAZ lidar system in a land-based mobile version with similar characteristics to the aircraft system [138].

Authors from York University/Environment Canada, Canada, and the Alfred Wegener Institute, Germany, reported on the development of an onboard DIAL lidar for measuring atmospheric ozone concentration. This lidar was installed on board a Polar 5 research aircraft to study ozone depletion over Arctic sea ice [139]. In this lidar, the fourth harmonic of a pulsed Nd:YAG laser (266 nm, 70 mJ per pulse, repetition rate 20 Hz) is focused into the center of a stimulated Raman scattering (SRS) cell filled with CO_2 at the pressure of 140 PSI to generate radiation with wavelengths of 276, 287, and 299 nm. The diameter of the multi-wavelength output beam was increased three times to reduce the divergence to about 0.2 mrad before it was directed into the atmosphere. The complete overlap between the emitted laser pulse and the telescope field of view occurred at a distance of 200 m. The signal received in this range was not used in ozone analysis. The DIAL system was installed in a single aircraft rack (56 × 64 × 130 cm), which is an autonomous unit with internal temperature control and a vibration isolation system. The laser and telescope are directed through a hatch made of two high-quality glass plates with UV-reflective coatings. The gap between the glass plates is filled with argon to prevent icing. A rack is attached to the seat rails, while the window is located above the opening, with exposure to the atmosphere under the aircraft [139].

Measurements using this lidar, conducted during a flight over the ice north of Barrow, Alaska, revealed ozone depletion in the surface layer at a distance of up to 300 km. Photochemical destruction of ground-level ozone was most intense at the northernmost point of the flight and steadily decreased towards land. All the ozone-depleted air observed during the flight was within 300 m of the sea ice surface. An analysis of the reverse trajectory of the air measured during the flight showed that air with a low ozone content formed above the ice. The study indicated a strong inverse correlation between the measured ozone concentration and the time of direct interaction of air with sea ice [139].

NASA Langley Research Center, USA, described the NASA DIAL compact on-board lidar for ozone measurement in small aircraft (B-200) and high-altitude aircraft (ER-2) [140]. The NASA DIAL lidar uses an Nd:YAG laser and a nonlinear optical module (NLO) with an OPO for sum frequency generation (SFG): combining OPO and 355 nm to obtain probing wavelengths of 290/300 nm in the onboard NASA DIAL lidar. The NLO consists of two OPOs and two SFG crystals. The pump laser is a single-frequency laser with a seed at a wavelength of 1064 nm, with one oscillator and one preamplifier. The result is two output beams with wavelengths of 290/300 nm and an energy of 100 mJ per pulse at a frequency of 200 Hz (20 W) at each output. The unique capabilities of the NASA DIAL lidar make it possible to clearly observe large-scale features of horizontal and vertical ozone distribution. The ozone profiles obtained with the lidar matched well with the profiles obtained with simultaneous launches of ozone probes. This was with an accuracy of up to 1.2% and an average deviation of 5.7% [140].

While Section 4.2 describes a DLR DIAL lidar with a wavelength of 935 nm for water vapor sensing [140,141], a modification of this lidar with the addition of an ultraviolet (UV) channel for ozone measurement is presented in the work of the authors at the DLR Institute of Atmospheric Physics, Germany. The DLR DIAL transmitter is based on a near-infrared OPO, whose frequency is converted to the UV range intracavity sum-frequency mixing to achieve continuous tuning in the UV wavelength range of 297–317 nm [141]. The average output power in this range exceeds 1 W, which corresponds to more than 10 mJ per pulse at a repetition rate of 100 Hz.

The DLR DIAL system for ozone measurement has been tested in both ground and onboard configurations. During the Wave-driven Isentropic Exchange (WISE) field campaign in 2017, the first simultaneously measured two-dimensional cross-sections of ozone and water vapor in the upper troposphere and lower stratosphere were obtained. This demonstrates the high potential of this system for studying exchange processes in this region of the atmosphere [141].

4.4.3. Brief Analysis

Table 5 summarizes the main characteristics of the above-described differential absorption lidars for ozone sensing [137–141].

Table 5. Airborne DIAL lidars for ozone sensing *.

Lidar System	Laser Source	Wavelength, nm	Laser Parameters	Telescope, m	Photodetector	Ranges, km	Reference
DIAL TOPAZ NOAA/ESRL, USA	Nd:YLF Ce:LiCAF	283–310	E = 0.1 mJ; f = 1 kHz; τ = 100 ns; Δλ = 0.2 nm	Newtonian 0.4	PMT	0.4 to 5, with resolution of 90 m	[137,138]
Arctic DIAL York Univ. Env. Canada Alf. Wegener Inst. Germany	Nd:YAG CO_2 BKP	276/ 287/ 299	E = 70 mJ; Δλ = 1 nm; f = 20 Hz; Θ = 0.2 mrad	Cassegrain 0.15	PMT	0.2 to 2.2, with resolution of 7.5 m	[139]
NASA DIAL NASA Langley Research Center, USA	Nd:YAG OPO	290/300	E = 100 mJ; f = 200 Hz; Δλ = 0.2 nm; Θ = 0.85 mrad	Newtonian 0.4	PMT	0.2 to 7	[140]
DLR DIAL, DLR Institute of Atm. Phys. Germany	OPO KTP Nd:YAG	297–317	E = 10 mJ; τ = 10 ns; f = 100 Hz Θ = 0.5 mrad	Cassegrain 0.48	APD PIN photodiodes	From 0.5 to 22	[141]

* E—energy in radiation pulse; Δλ—radiation line width (nm); τ—radiation pulse duration; f—pulse repetition frequency; Θ—laser radiation divergence.

From the review above regarding mobile ozone lidars, it follows that a lidar with a solid-state diode-pumped Nd:YAG laser with an energy of 0.1–100 mJ and a telescope (assembled by Newtonian or Cassegrain scheme) with a receiving mirror of 15–48 cm is promising for creating a modern compact mobile UV lidar system capable of ensuring a resolution to ozone monitoring problems in the altitude range from the surface layer to the troposphere with a high spatial resolution, short measurement time, and compulsory geopositioning system.

5. Results of the Development of Onboard Space Lidar Systems for Greenhouse Gas Sensing

5.1. History of Development

Satellite-based lidars can also be attributed to onboard lidars. The multi-wavelength space lidar project, developed by NASA Langley Research Center as part of the Shuttle Atmospheric Lidar System program after preliminary studies [142], was first proposed in 1979 [143].

The first operational space lidar was created at NASA to conduct research on aerosols and clouds in the atmosphere under the Lidar In-space Technology Experiment (LITE) program. It operated on the space shuttle Discovery in September 1994 [144].

The Russian lidar BALKAN was launched into space on the Spectrum module of the Mir space station in May 1995 [145]. Then, in 1996, the Russian–French lidar ALISSA was further delivered to the Mir station on the Priroda module [146].

From that point on, space lidar technologies developed primarily in the direction of research into aerosols and clouds in the atmosphere. This is the subject of a detailed review [16] and a monograph [147].

Limited work has been devoted to the development of onboard space lidar systems for greenhouse gas sensing. Right now, all projects and programs on this topic concerning aircraft prototypes of space lidars for greenhouse gas research are in the planning and development stage. This is described in Section 3 of this article.

The authors from NASA Goddard Space Flight Center, Greenbelt, USA, as part of the Active Sensing of CO_2 Emissions over Nights, Days and Seasons (ASCENDS) mission, proposed to create a pulsed two-wave lidar based on the IPDA method for measuring CO_2 concentration in the atmosphere [148–151].

It is also worth noting the Advanced Space Carbon and Climate Observation of Planet Earth (A-SCOPE) program, in which the European Space Agency authors planned to use the IPDA space lidar to study atmospheric CO_2 [,152].

Lidar technology was proposed in [153,154] for measuring gas components in Earth's and Mars' atmospheres.

5.2. Greenhouse Gas Lidar Developments in Recent Years

Global spatial and temporal measurements of greenhouse gas concentrations in the atmosphere are carried out as part of research using a space-based lidar for remote sensing of methane—the Methane Remote Sensing Lidar Mission (MERLIN) [16,26,155–157].

Lidar operates on the basis of DIAL/IPDA, and the project is the result of cooperation between France and Germany. It is aimed at launching and operating a satellite for monitoring atmospheric CH_4 [16,26,155–157].

The MERLIN lidar uses two separate telescopes to transmit and receive laser pulses. Both telescopes are installed on the same optical platform. This platform also includes a laser transmitter, a detection unit, and two star trackers for verification and guidance control.

The MERLIN lidar has a circumpolar sun-synchronous orbit (SSO) with an altitude of about 500 km. The MERLIN lidar is designed to measure the column methane content along the satellite's trajectory with a random error of less than 27 ppb (averaging over 50 km along the satellite's trajectory) and a systematic error of less than 3.7 ppb [16,26,155–157].

CO_2 emissions from powerful point sources, primarily large power plants, contribute significantly to total CO_2 emissions, so independent monitoring is essential.

The authors from the DLR Institute of Atmospheric Physics, Germany, reported on the development of a satellite lidar with double pulse and direct detection using IPDA. This lidar is capable of actively targeting point sources [158]. In their work, the required

characteristics of a lidar with an orbital altitude of 500 km were determined. In addition, the accuracy of detecting emission plumes using space lidar was evaluated.

The Gaussian plume model simulates CO_2 or CH_4 distribution downstream of point sources. It is shown that an IPDA lidar in a 500 km orbit with an average power of 2 W in the CO_2 absorption band at a wavelength of 1.6 μm, a pulse repetition frequency of 500 Hz, a coverage area of 50 m at sea level and a telescope diameter of 0.7 m is expected to be able to measure CO_2 and CH_4 emissions with an average accuracy of better than 3% at a distance up to 3 km from the source.

The work of Chinese authors from Zhejiang University, Hangzhou and the Chinese Academy of Science, Shanghai, analyzes the characteristics of the IPDA space lidar. This is part of the Aerosol and Carbon Detection Lidar (ACDL) developed in China [159]. The sources of random and systematic errors of the IPDA lidar at an orbit of 705 km were analyzed. The total systematic errors were 0.589 ppm. Based on data from September 2016, an average monthly global distribution of relative random errors was constructed. This distribution over a 16-day orbit repetition cycle showed a relatively uniform error distribution across the Northern Hemisphere. The results showed that 61.24% of the global error values were less than 0.25%, or about 1 ppm, while 2.76% of the values were greater than 0.75%. Statistical data allow us to assess the future capabilities of the IPDA space lidar [159].

ACDL was successfully launched on April 16, 2022, and has operated in orbit for more than one year, which achieved, for the first time, high-precision global measurement of XCO_2 and aerosol profiles. It is the first space-borne CO_2 detection lidar [160,161]. The lidar validated high-precision spaceborne data inversion during the in-orbit test, with a CO_2 column concentration measurement accuracy better than 0.7 ppm. In particular, for global greenhouse gas CO_2 concentration measurement, it obtained the first global CO_2 column concentration at night, and the first CO_2 column concentration in the bipolar zone, which is useful for global carbon source and sink estimation. In future, a satellite-ground campaign for XCO_2 measurements will be implemented, and data inversion methods will be improved.

5.3. Brief Analysis

Table 6 summarizes the main characteristics of the above-mentioned spaceborne IPDA greenhouse gas lidar systems [16,26,155–161].

Table 6. Spaceborne IPDA greenhouse gases lidars *.

Lidar System	Laser Source	Wavelength, nm	Laser Parameters	Telescope, m	Photodetector	Resolution, km	Reference
CH_4 IPDA MERLIN CNES/LMD/ LCSE, France DLR, Germany	OPO Nd:YAG	1645.552 1645.846	E = 9.5 mJ; τ = 20 ns; f = 20 Hz	Cassegrain 0.69	Avalanche Pin Diode (APD)	Horizontal: 50 vertical: total column	[16,26,155–157]
CO_2/CH_4 IPDA DLR, DLR Institute of Atm. Phys. Germany	OPO Nd:YAG	1570.0 2050.0 1650.0	E = 2 mJ; τ = 20 ns; f = 500 Hz	Cassegrain 0.7	APD HgCdTe InGaAs detectors	Horizontal: 10 vertical: total column	[158]
CO_2 IPDA Zhejiang University Chinese Academy of Science, China	DFB laser diodes	1572.024 1572.085	E = 75 mJ; τ = 15 ns; f = 20 Hz Δω = 50 MHz; Θ = 0.1 mrad	Cassegrain 1	InGaAs APD	Horizontal: 50 vertical: total column	[159–161]

* E—energy in radiation pulse; Δλ—radiation line width (nm); τ—radiation pulse duration; f—pulse repetition frequency; Θ—laser radiation divergence.

From Table 6 and the above description of the developments of spaceborne IPDA lidar systems for greenhouse gas sensing, the following conclusions can be drawn:

(1) The CO_2/CH_4 IPDA lidars described above operate either in a fairly strong CO_2 absorption band of 2 μm, or in a weaker CO_2/CH_4 absorption band of 1.57/1.65 μm;

(2) For greenhouse gas sensing using spaceborne lidars, OPO Nd:YAG lasers are used, which allows for the generation of wavelengths in the near-IR range in the region of a CO_2 absorption band of about 1.57 μm nm. Less often, OPO Nd:YAG lasers are used to operate in the region of the CO_2 absorption band of about 2 μm or DFB laser diodes in 1.57 μm;

(3) The receiving optics in greenhouse gas lidars are represented by Cassegrain telescopes with a diameter of 0.69–1 m;

(4) Spaceborne methane lidars use various semiconductor photodiodes as receivers, with peak sensitivity in the region of the probing laser radiation;

(5) In space lidars with an orbital altitude of 500–700 km, the IPDA methodology is used to measure greenhouse gas column content with a horizontal resolution of 10–50 km.

6. Conclusions

Due to the possible use of onboard equipment in hard-to-reach regions and the full coverage of tropospheric heights during experiments, it is extremely critical to study greenhouse gases using onboard lidar equipment.

The CO_2 lidars described above operate either in a fairly strong carbon dioxide absorption band of 2 μm, or in a weaker absorption band of 1.57 μm. For CO_2 sensing using airborne mobile lidars, DFB lasers with lower energy are most often used, which allows for the generation of wavelengths in the near-IR range in the region of a CO_2 absorption band of about 1.57 μm. Less often, Ho:Tm:YLF or OPO Nd:YAG lasers are used to operate in the region of the carbon dioxide absorption band of about 2 μm.

The H_2O lidars operate either in a fairly strong water vapor absorption band of 2 μm, or in a weaker absorption band of 935 nm. For H_2O sensing using airborne mobile lidars, OPO Nd:YAG lasers are used, which allows for the generation of wavelengths in the near-IR range in the region of a water vapor absorption band of about 935 nm. Less often, Ho:Tm:YLF lasers are used to operate in the region of the water vapor absorption band of about 2 μm.

The CH_4 lidars operate either in a fairly strong water vapor absorption band of 3 μm, or in a weaker absorption band of 1.65 μm. For CH_4 sensing using airborne mobile lidars, OPO Nd:YAG lasers are used, which allows for the generation of wavelengths in the near-IR range in the region of a water vapor absorption band of about 1.65 μm. Less often, OPO Nd:YAG lasers are used to operate in the region of the water vapor absorption band of about 3 μm.

From the review above regarding mobile ozone lidars, it follows that a lidar with a solid-state diode-pumped Nd:YAG laser with a repetition rate of 20 Hz and an energy of 30 mJ, and a telescope (assembled by the Newtonian or Cassegrain scheme) with a receiving mirror of 30–50 cm, is promising for creating a modern compact mobile UV lidar system capable of ensuring a resolution to ozone monitoring problems in the altitude range from the surface layer to the troposphere with a high spatial resolution, short measurement time, and compulsory geopositioning system.

For greenhouse gas sensing using spaceborne lidars, OPO Nd:YAG lasers are used, which allows for the generation of wavelengths in the near-IR range in the region of a CO_2 absorption band of about 1.57 μm nm. Less often, OPO Nd:YAG lasers are used to operate in the region of the CO_2 absorption band of about 2 μm or DFB laser diodes in

1.57 μm. Spaceborne methane lidars use various semiconductor photodiodes as receivers, with peak sensitivity in the region of the probing laser radiation. In space lidars with an orbital altitude of 500–700 km, the IPDA methodology is used to measure greenhouse gas column content with a horizontal resolution of 10–50 km.

Lidar onboard systems provide, in contrast to standard gas analysis systems, undoubted advantages in quickly obtaining the necessary data in a non-contact way to study the atmosphere's gas composition.

The onboard DIAL/IPDA lidar systems described in this review are capable of large-scale mapping and quantification of the content of major greenhouse gases (H_2O, CO_2, CH_4 and O_3) in the atmosphere of various climate zones.

Author Contributions: Conceptualization, O.A.R.; methodology, S.V.Y., S.A.S. and A.A.N.; software, S.A.S. and A.A.N.; formal analysis, O.A.R. and S.V.Y.; investigation, S.V.Y., S.A.S., O.V.K., A.V.N., A.A.N. and N.S.K.; writing—review and editing, O.A.R. and S.V.Y.; visualization, O.V.K., A.V.N. and A.A.N.; supervision, O.A.R.; project administration, O.A.R. and S.V.Y.; funding acquisition, O.A.R. and S.V.Y. All authors have read and agreed to the published version of the manuscript.

Funding: This study was supported by the Ministry of Science and Higher Education of the Russian Federation (budget funds for IAO SB RAS).

Data Availability Statement: The original contributions presented in this study are included in the article/Supplementary Material. Further inquiries can be directed to the corresponding author.

Conflicts of Interest: The authors declare no conflicts of interest.

References

1. McNutt, M. Times's up, CO_2. *Science* **2019**, *365*, 411. https://doi.org/10.1126/science.aay8827.
2. George, S.S. The aberrant global synchrony of present-day warming. *Nature* **2019**, *571*, 483–484. https://doi.org/10.1038/d41586-019-02179-2.
3. Neukom, R.; Steiger, N.; Gómez-Navarro, J.J.; Wang, J.; Werner, J.P. No evidence for globally coherent warm and cold periods over the preindustrial Common Era. *Nature* **2019**, *571*, 550–554. https://doi.org/10.1038/s41586-019-1401-2.
4. Shepherd, T.G. Effects of a warming Arctic. *Science* **2016**, *353*, 989–990. https://doi.org/10.1126/science.aag2349.
5. Johannessen, O.M.; Kuzmina, S.I.; Bobylev, L.P.; Miles, M.W. Surface air temperature variability and trends in the Arrctic: New amplification assessment and regionalisation. *Tellus* **2016**, *68*, 28234. https://doi.org/10.3402/tellusa.v68.28234.
6. Vasil'ev, B.I.; Mannoun, U.M. IR differential-absorption lidars for ecological monitoring of the environment. *Quantum Electron.* **2006**, *36*, 801–820. https://doi.org/10.1070/QE2006v036n09ABEH006577.
7. Bobrovnikov, S.M.; Matvienko, G.G.; Romanovskii, O.A.; Serikov, I.B.; Sukhanov, A.Y. *Spectroscopic Lidar Gas Analysis of Atmosphere*; IAO SB RAS: Tomsk, Russia, 2014; 510 p.
8. Balin, Y.S.; Borovoy, A.G.; Burlakov, V.D.; Dolgii, S.I.; Klemasheva, M.G.; Konoshonkin, A.V.; Kokhanenko, G.P.; Kustova, N.V.; Marichev, V.N.; Matvienko, G.G.; et al. *Lidar Monitoring of Cloud and Aerosol Particles, Trace Gases and Meteorological Parameters of the Atmosphere*; Publishing house of the IAO SB RAS: Tomsk, Russia, 2015; 450 p.
9. Boreysho, A.S.; Kim, A.A.; Konyaev, M.A.; Luginya, V.S.; Morozov, A.V.; Orlov, A.E. Modern Lidar Systems for Atmosphere Remote Sensing. *Photonics Russ.* **2019**, *7*, 648–657.
10. Griffith, D.W.T.; Pohler, D.; Schmitt, S.; Hammer, S.; Vardag, S.N.; Platt, U. Long open-path measurements of greenhouse gases in air using near-infrared Fourier transform spectroscopy. *Atmos. Meas. Tech.* **2018**, *11*, 1549–1563. https://doi.org/10.5194/amt-2017-272.
11. Kistenev, Y.V.; Cuisset, A.; Romanovskii, O.A.; Zherdeva, A.V. A Study of Trace Atmospheric Gases at the Water–Atmosphere Interface Using Remote and Local IR Laser Gas Analysis: A Review. *Atmos. Ocean. Opt.* **2022**, *35*, S17–S29. https://doi.org/10.1134/S1024856023010074.
12. Molebny, V.; McManamon, P.F.; Steinvall, O.; Kobayashi, T.; Chen, W. Laser radar: Historical prospective—From the East to the West. *Opt. Eng.* **2016**, *56*, 031220. https://doi.org/10.1117/1.OE.56.3.031220.
13. Li, N.; Ho, C.P.; Xue, J.; Lim, L.W.; Chen, G.; Fu, Y.H.; Lee, L.Y.T. A Progress Review on Solid-State LiDAR and Nanophotonics-Based LiDAR Sensors. *Laser Photonics Rev.* **2022**, *16*, 2100511. https://doi.org/10.1002/lpor.202100511.

14. Tyagi, L.; Devi, R.; Tyagi, S.; Kumar, V.; Sharma, K.; Gautam, Y.K.; Kumar, A.; Kapoor, S.; Bhardwaj, A.; Kumar, A. Environmental Impacts and Recent Advancements in the Sensing of Methane: A Review. *Environ. Technol. Rev.* **2025**, *14*, 191–212. https://doi.org/10.1080/21622515.2025.2470448.
15. Li, J.; Yu, Z.; Du, Z.; Ji, Y.; Liu, C. Standoff Chemical Detection Using Laser Absorption Spectroscopy: A Review. *Remote Sens.* **2020**, *12*, 2771. https://doi.org/10.3390/rs12172771.
16. Bolcek, J.; Gibril, M.B.A.; Veverka, J.; Sloboda, Š.; Maršálek, R.; Götthans, T. Spaceborne LiDAR Systems: Evolution, Capabilities, and Challenges. *Sensors* **2025**, *25*, 3696. https://doi.org/10.3390/s25123696.
17. Talnikar, V.D.; Kulkarni, S.J. An Open Review on Air Pollution Monitoring Systems. *Environ. Technol. Rev.* **2025**, *14*, 910–932. https://doi.org/10.1080/21622515.2025.2542579.
18. Romanovskii, O.A.; Yakovlev, S.V.; Sadovnikov, S.A.; Nevzorov, A.A.; Nevzorov, A.V.; Kharchenko, O.V.; Kravtsova, N.S.; Kistenev, Y.V. Ground-based Stationary Differential Absorption Lidars for Monitoring Greenhouse Gases in the Atmosphere. *Atmos. Ocean. Opt.* **2025**, *38*, 345–359. https://doi.org/10.1134/S1024856025700150.
19. Romanovskii, O.A.; Kistenev, Y.V.; Yakovlev, S.V.; Nevzorov, A.A.; Nevzorov, A.V.; Sadovnikov, S.A.; Kharchenko, O.V. Mobile ground-based differential absorption lidar systems for atmospheric greenhouse gas sensing: A review. *Appl. Spectrosc. Rev.* **2025**, *61*, 165–211. https://doi.org/10.1080/05704928.2025.2508822.
20. Moiseenko, K.B.; Shtabkin, Y.A.; Vasileva, A.V.; Skorokhod, A.I.; Fedorova, E.I. Regional Sources and CH_4 Seasonal Cycle in Central Siberia and the Arctic: Observations and Numerical Calculations. *Atmos. Ocean. Opt.* **2024**, *37*, 82–93. https://doi.org/10.1134/S1024856023700100.
21. Defratyka, S.M.; Paris, J.-D.; Yver-Kwok, C.; Loeb, D.; France, J.; Helmore, J.; Yarrow, N.; Gros, V.; Bousquet, P. Ethane measurement by Picarro CRDS G2201-i in laboratory and field conditions: Potential and limitations. *Atmos. Meas. Tech.* **2021**, *14*, 5049–5069. https://doi.org/10.5194/amt-14-5049-2021.
22. Gorka, M.; Bezyk, Y.; Sowka, I. Assessment of GHG interactions in the vicinity of the municipal waste landfill site-case study. *Energies* **2021**, *14*, 8259. https://doi.org/10.3390/en14248259.
23. Bezyk, Y.; Sowka, I.; Gorka, M.; Blachowski, J. GIS-based approach to spatio-temporal interpolation of atmospheric CO_2 concentrations in limited monitoring dataset. *Atmosphere* **2021**, *12*, 384. https://doi.org/10.3390/atmos12030384.
24. Zhao, Z.; He, Q.; Lu, Z.; Zhao, Q.; Wang, J. Analysis of atmospheric CO_2 and CO at Akedala Atmospheric Background Observation Station, a Regional Station in Northwestern China. *Int. J. Environ. Res. Public Health* **2022**, *19*, 6948. https://doi.org/10.3390/ijerph19116948.
25. Twigg, M.M.; Berkhout, A.J.C.; Cowan, N.; Crunaire, S.; Dammers, E.; Ebert, V.; Gaudion, V.; Haaima, M.; Häni, C.; John, L.; et al. Intercomparison of in situ measurements of ambient NH_3: Instrument performance and application under field conditions. *Atmos. Meas. Tech.* **2022**, *15*, 6755–6787. https://doi.org/10.5194/amt-15-6755-2022.
26. Jiang, Y.; Zhang, L.; Zhang, X.; Cao, X. Methane retrieval algorithms based on satellite: A review. *Atmosphere* **2024**, *15*, 449. https://doi.org/10.3390/atmos15040449.
27. Shimoda, H.; Ogawa, T. Interferometric Monitor for Greenhouse Gases (IMG). *Adv. Space Res.* **2000**, *25*, 937–946. https://doi.org/10.1016/S0273-1177(99)00926-6.
28. Berndt, E.B.; Smith, N.; Barnet, C.D. Integrating NASA Aqua AIRS in a Real-Time NUCAPS Science-To-Applications System to Support Severe Weather Forecasting. *Earth Space Sci.* **2023**, *10*, e2022EA002725. https://doi.org/10.1029/2022EA002725.
29. Kulawik, S.S.; Jones, D.B.A.; Nassar, R.; Irion, F.W.; Worden, J.R.; Bowman, K.W.; Machida, T.; Matsueda, H.; Sawa, Y.; Biraud, S.C.; et al. Characterization of Tropospheric Emission Spectrometer (TES) CO_2 for carbon cycle science. *Atmos. Chem. Phys.* **2010**, *10*, 5601–5623. https://doi.org/10.5194/acp-10-5601-2010.
30. Clerbaux, C.; Hadji-Lazaro, J.; Turquety, S.; George, M.; Boynard, A.; Pommier, M.; Safieddine, S.; Coheur, P.F.; Hurtmans, D.; Clarisse, L.; et al. Tracking pollutants from space: Eight years of IASI satellite observation. *Comptes Rendus Geosci.* **2015**, *347*, 134–144. https://doi.org/10.1016/j.crte.2015.06.001.
31. Bergamaschi, P.; Frankenberg, C.; Meirink, J.F.; Krol, M.; Dentener, F.; Wagner, T.; Platt, U.; Kaplan, J.O.; Körner, S.; Heimann, M.; et al. Satellite chartography of atmospheric methane from SCIAMACHY on board ENVISAT: 2. Evaluation based on inverse model simulations. *J. Geophys. Res.* **2007**, *112*, D02304. https://doi.org/10.1029/2006JD007268.
32. Kikuchi, N.; Yoshida, Y.; Uchino, O.; Morino, I.; Yokota, T. An advanced retrieval algorithm for greenhouse gases using polarization information measured by GOSAT TANSO-FTS SWIR I: Simulation study. *J. Geophys. Res. Atmos.* **2016**, *121*, 13,129–13,157. https://doi.org/10.1002/2015JD024720.

33. Hu, H.; Landgraf, J.; Detmers, R.; Borsdorff, T.; de Brugh, J.A.; Aben, I.; Butz, A.; Hasekamp, O. Toward global mapping of methane with TROPOMI: First results and intersatellite comparison to GOSAT. *Geophys. Res. Lett.* **2018**, *45*, 3682–3689. https://doi.org/10.1002/2018GL077259.
34. Noël, S.; Reuter, M.; Buchwitz, M.; Borchardt, J.; Hilker, M.; Schneising, O.; Bovensmann, H.; Burrows, J.P.; Di Noia, A.; Parker, R.J.; et al. Retrieval of Greenhouse Gases from GOSAT and GOSAT-2 Using the FOCAL Algorithm. *Atmos. Meas. Tech.* **2022**, *15*, 3401–3437. https://doi.org/10.5194/amt-15-3401-2022.
35. Luo, H.; Li, Z.; Wu, Y.; Qiu, Z.; Shi, H.; Wang, Q.; Xiong, W. Greenhouse Gases Monitoring Instrument on GaoFen-5 Satellite-II: Optical Design and Evaluation. *Remote Sens.* **2023**, *15*, 1105. https://doi.org/10.3390/rs15041105.
36. Tanimoto, H.; Matsunaga, T.; Someya, Y.; Fujinawa, T.; Ohyama, H.; Morino, I.; Yashiro, H.; Sugita, T.; Inomata, S.; Müller, A.; et al. The greenhouse gas observation mission with Global Observing SATellite for Greenhouse gases and Water cycle (GOSAT-GW): Objectives, conceptual framework and scientific contributions. *Prog. Earth Planet. Sci.* **2025**, *12*, 8. https://doi.org/10.1186/s40645-025-00684-9.
37. Sierk, B.; Fernandez, V.; Bezy, J.-L.; Meijer, Y.; Durand, Y.; Courrèges-Lacoste, G.B.; Pachot, C.; Löscher, A.; Nett, H.; Minoglou, K.; et al. *The Copernicus CO2M Mission for Monitoring Anthropogenic Carbon Dioxide Emissions from Space*; International Conference on Space Optics: Bellingham, WA, USA, 2021; Volume 11852, p. 118523M-1–118523M-18. https://doi.org/10.1117/12.2599613.
38. White, E.; Shephard, M.W.; Cady-Pereira, K.E.; Kharol, S.K.; Ford, S.; Dammers, E.; Chow, E.; Thiessen, N.; Tobin, D.; Quinn, G.; et al. Accounting for non-detects: Application to satellite ammonia observations. *Remote Sens.* **2023**, *15*, 2610. https://doi.org/10.3390/rs15102610.
39. Zhou, M.; Deng, Z.; Robert, C.; Zhang, X.; Zhang, L.; Wang, Y.; Qi, C.; Wang, P.; De Mazière, M. The first global map of atmospheric ammonia (NH_3) as observed by the HIRAS/FY-3D satellite. *Adv. Atmos. Sci.* **2024**, *41*, 379–390. https://doi.org/10.1007/s00376-023-3059-9.
40. Irakulis-Loitxate, I.; Gorroño, J.; Zavala-Araiza, D.; Guanter, L. Satellites detect a methane ultra-emission event from an offshore platform in the Gulf of Mexico. *Environ. Sci. Technol. Lett.* **2022**, *9*, 520–525. https://doi.org/10.1021/acs.estlett.2c00225.
41. Chalinel, R.; Attie, J.-L.; Ricaud, P.; Vidot, J.; Kangah, Y.; Hauglustaine, D.; Thompson, R. Evaluation and global-scale observation of nitrous oxide from IASI on Metop-A. *Remote Sens.* **2022**, *14*, 1403. https://doi.org/10.3390/rs14061403.
42. Gao, R. Research progress of atmospheric CO_2 monitoring by satellite remote sensing. *J. Phys. Conf. Ser.* **2022**, *2386*, 012028. https://doi.org/10.1088/1742-6596/2386/1/012028.
43. Huang, Y.; Wei, J.; Jin, J.; Zhou, Z.; Gu, Q. CO Fluxes in Western Europe during 2017–2020 Winter seasons inverted by WRF-Chem/Data assimilation research testbed with MOPITT observations. *Remote Sens.* **2022**, *14*, 1133. https://doi.org/10.3390/rs14051133.
44. Gaubert, B.; Edwards, D.P.; Anderson, J.L.; Arellano, A.F.; Barré, J.; Buchholz, R.R.; Darras, S.; Emmons, L.K.; Fillmore, D.; Granier, C.; et al. Global scale inversions from MOPITT CO and MODIS AOD. *Remote Sens.* **2023**, *15*, 4813. https://doi.org/10.3390/rs15194813.
45. Batchelor, R.L.; Strong, K.; Lindenmaier, R.; Mittermeier, R.L.; Fast, H.; Drummond, J.R.; Fogal, P.F. A new Bruker IFS 125HR FTIR spectrometer for the polar environment atmospheric research laboratory at Eureka, Nunavut, Canada: Measurements and comparison with the existing Bomem DA8 spectrometer. *J. Atmos. Ocean. Technol.* **2009**, *26*, 1328–1340. https://doi.org/10.1175/2009JTECHA1215.1.
46. Makarova, M.V.; Serdyukov, V.I.; Arshinov, M.Y.; Belan, B.D.; Voronin, B.A.; Nikitin, A.V.; Shcherbakov, A.P.; Gridnev, Y.V. The First Complex Experiment on Determining Parameters of the Vertical Distribution of Methane in the Troposphere over Western Siberia from Solar Spectra Recorded with an IFS-125M FTIR Spectrometer and In Situ Aircraft Measurements. *Atmos. Ocean. Opt.* **2021**, *34*, 61–67. https://doi.org/10.1134/S1024856021010073.
47. Gisi, M.; Hase, F.; Dohe, S.; Blumenstock, T.; Simon, A.; Keens, A. XCO_2-measurements with a tabletop FTS using solar absorption spectroscopy. *Atmos. Meas. Tech.* **2012**, *5*, 2969–2980. https://doi.org/10.5194/amt-5-2969-2012.
48. Wiacek, A.; Taylor, J.R.; Strong, K.; Saari, R.; Kerzenmacher, T.E.; Jones, N.B.; Griffith, D.W.T. Ground-Based solar absorption FTIR spectroscopy: Characterization of retrievals and first results from a novel optical design instrument at a New NDACC Complementary Station. *J. Atmos. Ocean. Technol.* **2007**, *24*, 432–448.
49. Makarova, M.; Poberovskiy, A.; Hase, F.; Timofeyev, Y.M.; Imhasin, K.K. Determination of the Characteristics of Ground-Based IR Spectral Instrumentation for Environmental Monitoring of the Atmosphere. *J. Appl. Spectrosc.* **2016**, *83*, 429–436. https://doi.org/10.1007/s10812-016-0306-1.

50. Gisi, M.; Hase, F.; Dohe, S.; Blumenstock, T. Camtracker: A new camera controlled high precision solar tracker system for FTIR-spectrometers. *Atmos. Meas. Tech.* **2011**, *4*, 47–54. https://doi.org/10.5194/amt-4-47-2011.
51. Baidar, S.; Kille, N.; Ortega, I.; Sinreich, R.; Thomson, D.; Hannigan, J.; Volkamer, R. Development of a digital mobile solar tracker. *Atmos. Meas. Tech.* **2016**, *9*, 963–972. https://doi.org/10.5194/amt-9-963-2016.
52. Robinson, J.; Smale, D.; Pollard, D.; Shiona, H. Solar tracker with optical feedback and continuous rotation. *Atmos. Meas. Tech.* **2020**, *13*, 5855–5871. https://doi.org/10.5194/amt-13-5855-2020.
53. Bezanilla, A.; Krüger, A.; Stremme, W.; Grutter, M. Solar absorption infrared spectroscopic measurements over Mexico City: Methane enhancements. *Atmósfera* **2014**, *27*, 173–183.
54. Chelin, P.; Viatte, C.; Ray, M.; Eremenko, M.; Cuesta, J.; Hase, F.; Orphal, J.; Flaud, J.-M. The OASIS Observatory Using Ground-Based Solar Absorption Fourier-Transform Infrared Spectroscopy in the Suburbs of Paris (Créteil-France). In *Environment, Energy and Climate Change I: Environmental Chemistry of Pollutants and Wastes*; Springer: Cham, Switzerland, 2015; pp. 21–52. https://doi.org/10.1007/698_2014_270.
55. . Deng, Y.; Xu, L.; Sheng, X. et al. Vehicle-Mounted Solar Occultation Flux Fourier Transform Infrared Spectrometer and Its Remote Sensing Application. *Sensors* 2023, *23*(9), 4317. https://doi.org/10.3390/s23094317.
56. Hase, F.; Frey, M.; Kiel, M.; Blumenstock, T.; Harig, R.; Keens, A.; Orphal, J. Addition of a channel for XCO observations to a portable FTIR spectrometer for greenhouse gas measurements. *Atmos. Meas. Tech.* **2016**, *9*, 2303–2313. https://doi.org/10.5194/amt-9-2303-2016.
57. Merlaud, A.; De Maziere, M.; Hermans, C.; Cornet, A. Equations for solar tracking. *Sensors* **2012**, *12*, 4074–4090. https://doi.org/10.3390/s120404074.
58. Notholt, J.; Schrems, O. Ground-based FTIR spectroscopic absorption measurements of stratospheric trace gases in the Arctic with the sun and the moon as light sources. *J. Mol. Struct.* **1995**, *347*, 407–416.
59. Hase, F.; Frey, M.; Blumenstock, T.; Groß, J.; Kiel, M.; Kohlhepp, R.; Tsidu, G.M.; Schäfer, K.; Sha, M.K.; Orphal, J. Application of portable FTIR spectrometers for detecting greenhouse gas emissions of the major city Berlin. *Atmos. Meas. Tech.* **2015**, *8*, 3059–3068. https://doi.org/10.5194/amt-8-3059-2015.
60. Wu, P.; Shan, C.; Liu, C.; Xie, Y.; Wang, W.; Zhu, Q.; Zeng, X.; Liang, B. Ground-Based Remote Sensing of Atmospheric Water Vapor Using High-Resolution FTIR Spectrometry. *Remote Sens.* **2023**, *15*, 3484. https://doi.org/10.3390/rs15143484.
61. Romanovskii, O.A.; Kharchenko, O.V.; Yakovlev, S.V. Methodological aspects of lidar ranging of trace gases in the atmosphere by differential absorption. *J. Appl. Spectrosc.* **2012**, *79*, 793–800. https://doi.org/10.1007/s10812-012-9673-4.
62. Collis, R.T.H.; Russell, P.B. Lidar Measurement of Particles and Gases by Elastic Backscattering and Differential Absorption. In *Laser Monitoring of the Atmosphere*; Hinkley, E.D., Ed.; Springer: New York, NY, USA, 1976; pp. 91–180.
63. Measures, R.M. *Laser Remote Sensing: Fundamentals and Applications*; Krieger Publishing Company: Malabar, FL, USA, 1992; 510 p.
64. Ehret, G.; Kiemle, C.; Wirth, M.; Amediek, A.; Fix, A.; Houweling, S. Space-borne remote sensing of CO_2, CH_4, and N_2O by integrated path differential absorption lidar: A sensitivity analysis. *Appl. Phys. B* **2008**, *90*, 593–608. https://doi.org/10.1007/s00340-007-2892-3.
65. Babchenko, S.V.; Matvienko, G.G.; Sukhanov, A.Y. Assessing the possibilities of sensing CH_4 and CO_2 greenhouse gases above the underlying surface with satellite-based IPDA lidar. *Atmos. Ocean. Opt.* **2015**, *28*, 245–253. https://doi.org/10.1134/S1024856015030045.
66. Matvienko, G.G.; Sukhanov, A.Y. Application of Neural Networks for Retrieval of the CO_2 Concentration at Aerospace Sensing by IPDA-DIAL lidar. *Remote Sens.* **2019**, *11*, 659. https://doi.org/10.3390/rs11060659.
67. Browell, E.V.; Dobbs, M.E.; Dobler, J.; Kooi, S.; Choi, Y.; Harrison, F.W.; Moore, B., III; Zaccheo, T.S. Airborne demonstration of 1.57-micron laser absorption spectrometer for atmospheric CO_2 measurements. Presented at the 24th International Laser Radar Conference, Boulder, Colorado, 23–24 June 2008.
68. Browell, E.V.; Dobbs, M.E.; Dobler, J.; Kooi, S.A.; Choi, Y.; Harrison, F.W.; Moore, I.I.I.B.; Zaccheo, T.S. First Airborne Laser Remote Measurements of Atmospheric Carbon Dioxide for Future Active Sensing of Carbon Dioxide from Space. *Geophys. Res. Abstr.* **2009**, *11*, EGU2009-2615.
69. Dobbs, M.E.; Dobler, J.; Braun, M.; McGregor, D.; Overbeck, J.; Moore, B., III; Browell, E.V.; Zaccheo, T. A Modulated CW Fiber Laser-Lidar Suite for the ASCENDS Mission. Presented at the 24th International Laser Radar Conference, Boulder, Colorado, 23–24 June 2008.
70. Dobbs, M.E.; Sharp, W.; Browell, E.V.; Zaccheo, S.; Moore, I.I.I.B. A sinusoidal modulated CW integrated path differential absorption lidar for mapping sources and sinks of carbon dioxide from space. In Proceedings of the 14th Coherent Laser Radar Conference, Snowmass, CO, USA, 8–13 July 2007.

71. Dobler, J.T.; Harrison, F.W.; Browell, E.V.; Lin, B.; McGregor, D.; Kooi, S.; Choi, Y.; Ismail, S. Atmospheric CO_2 column measurements with an airborne intensity-modulated continuous-wave 1.57 μm fiber laser lidar. *Appl. Opt.* **2013**, *52*, 2874–2892. https://doi.org/10.1364/AO.52.002874.
72. Kawa, S.; Abshire, J.; Baker, D.; Browell, E.; Crisp, D.; Crowell, S.; Hyon, J.; Jacob, J.; Jucks, K.W.; Lin, B.; et al. *Active Sensing of CO_2 Emissions over Nights, Days, and Seasons (ASCENDS): Final Report of the ASCENDS Ad Hoc Science Definition Team*; NASA/TP–2018-219034; Goddard Space Flight Center Greenbelt: Greenbelt, MD, USA, 2018; p. 20771.
73. Abshire, J.B.; Riris, H.; Allan, G.R.; Weaver, C.J.; Mao, J.; Sun, X.; Hasselbrack, W.E.; Kawa, S.R.; Biraud, S. Pulsed airborne lidar measurements of atmospheric CO_2 column absorption. *Tellus* **2010**, *62*, 770–783. https://doi.org/10.1111/j.1600-0889.2010.00502.x.
74. Spiers, G.D.; Menzies, R.T.; Jacob, J.; Christensen, L.E.; Phillips, M.W.; Choi, Y.; Browell, E.V. Atmospheric CO_2 measurements with a 2 μm airborne laser absorption spectrometer employing coherent detection. *Appl. Opt.* **2011**, *50*, 2098–2111. https://doi.org/10.1364/AO.50.002098.
75. Menzies, R.T.; Spiers, G.D.; Jacob, J.C. Airborne laser absorption spectrometer measurements of atmospheric CO_2 column mole fractions: Source and sink detection and environmental impact son retrievals. *J. Atmos. Ocean. Technol.* **2014**, *31*, 404–421. https://doi.org/10.1175/JTECH-D-13-00128.1.
76. Fix, A.; Amediek, A.; Büdenbender, C.; Ehret, G.; Quatrevalet, M.; Wirth, M.; Löhring, J.; Kasemann, R.; Klein, J.; Hoffmann, H.-D.; et al. Development and First Results of a new Near-IR Airborne Greenhouse Gas Lidar. In Proceedings of the Advanced Solid State Lasers Conference, Berlin, Germany, 4–9 October 2015; OSA Technical Digest, Paper ATh1A.2. https://doi.org/10.1364/EE.2015.EM3A.3.
77. Fix, A.; Amediek, A.; Bovensmann, H.; Ehret, G.; Gerbig, C.; Gerilowski, K.; Pfeilsticker, K.; Roiger, A.; Zöger, M. CoMet: An airborne mission to simultaneously measure CO_2 and CH_4 using lidar, passive remote sensing, and in-situ techniques. *EPJ Web Conf.* **2018**, *176*, 02003. https://doi.org/10.1051/epjconf/201817602003.
78. Amediek, A.; Ehret, G.; Fix, A.; Wirth, M.; Büdenbender, C.; Quatrevalet, M.; Kiemle, C.; Gerbig, C. CHARM-F—A new airborne integrated-path differential-absorption lidar for carbon dioxide and methane observations: Measurement performance and quantification of strong point source emissions. *Appl. Opt.* **2017**, *56*, 5182–5197. https://doi.org/10.1364/AO.56.005182.
79. Amediek, A.; Ehret, G.; Fix, A.; Wirth, M.; Büdenbender, C.; Quatrevalet, M.; Kiemle, C. Performance of Charm-F—The Airborne Demonstrator for Merlin. *EPJ Web Conf.* **2018**, *176*, 01002. Available online: https://www.researchgate.net/publication/324501199_Performance_of_Charm-F_-_the_airborne_demonstrator_for_Merlin (accessed on 15 November 2026).
80. Amediek, A.; Fix, A.; Ehret, G.; Caron, J.; Durand, Y. Airborne lidar reflectance measurements at 1.57 μm in support of the A-SCOPE mission for atmospheric CO_2. *Atmos. Meas. Tech.* **2009**, *2*, 755–772. https://doi.org/10.5194/amt-2-755-2009.
81. Sakaizawa, D.; Kawakami, S.; Nakajima, M.; Tanaka, T.; Morino, I.; Uchino, O. An airborne amplitude-modulated 1.57 μm differential laser absorption spectrometer: Simultaneous measurement of partial column-averaged dry air mixing ratio of CO_2 and target range. *Atmos. Meas. Tech.* **2013**, *6*, 387–396. https://doi.org/10.5194/amt-6-387-2013.
82. Kameyama, S.; Imaki, M.; Hirano, Y.; Ueno, S.; Kawakami, S.; Sakaizawa, D.; Nakajima, M. Performance improvement and analysis of a 1.6μm continuous-wave modulation laser absorption spectrometer system for CO_2 sensing. *Appl. Opt.* **2011**, *50*, 1560–1569. https://doi.org/10.1364/AO.50.001560.
83. Sakaizawa, D.; Nagasawa, C.; Nagai, T.; Abo, M.; Shibata, Y.; Nakazato, M.; Sakai, T. Development of a 1.6μm differential absorption lidar with a quasi-phase matching OPO and photon-counting detector for the vertical CO_2 profile. *Appl. Opt.* **2009**, *48*, 748–757. https://doi.org/10.1364/AO.48.000748.
84. Mao, J.; Abshire, J.; Kawa, S.; Sun, X.; Riris, H. Airborne Lidar Measurements of Atmospheric CO_2 Column Concentrations to Cloud Tops made during the 2017 ASCENDS/ABoVE Campaign. *Atmos. Meas. Tech.* **2024**, *17*, 1061–1074. https://doi.org/10.5194/amt-17-1061-2024.
85. Abshire, J.; Ramanathan, A.; Riris, H.; Allan, G.; Sun, X.; Hasselbrack, W.; Mao, J.; Wu, S.; Chen, J.; Numata, K.; et al. Airborne measurements of CO_2 column concentrations made with a pulsed IPDA lidar using a multiple-wavelength-locked laser and HgCdTe APD detector. *Atmos. Meas. Tech.* **2018**, *11*, 2001–2025. https://doi.org/10.5194/amt-11-2001-2018.
86. Abshire, J.; Ramanathan, A.; Riris, H.; Mao, J.; Allan, G.R.; Hasselbrack, W.E.; Weaver, C.J.; Browell, E.V. Airborne measurements of CO_2 column concentration and range using a pulsed direct detection IPDA lidar. *Remote Sens.* **2013**, *6*, 443–469. https://doi.org/10.3390/rs6010443.

87. Abshire, J.B.; Riris, H.; Weaver, C.; Mao, J.; Allan, G.; Hasselbrack, W.; Browell, E. Airborne measurements of CO_2 col umn absorption and range using a pulsed direct-detection inte grated path differential absorption lidar. *Appl. Opt.* **2013**, *52*, 4446–4461. https://doi.org/10.1364/AO.52.004446.
88. Refaat, T.; Singh, U. Carbon Dioxide Active Remote Sensing Using Pulsed 2-μm Lidar. In *Space-Based Lidar Remote Sensing Techniques and Emerging Technologies, Proceedings of the 3rd International Space Lidar Workshop*; Springer: Cham, Switzerland, 2024; pp. 73–86. https://doi.org/10.1007/978-3-031-53618-2_7.
89. Singh, U.; Refaat, T.; Reithmaier, K.; Yu, J.; Petros, M.; Remus, R.; Fay, J. Column CO_2 measurement from an airborne solid state double-pulsed 2-micron integrated path differential absorption lidar. In *International Conference on Space Optics—ICSO 2014*; SPIE: Bellingham, WA, USA, 2017; Volume 10563, 105630C. https://doi.org/10.1117/12.2304210.
90. Refaat, T.F.; Singh, U.N.; Yu, J.; Petros, M.; Remus, R.; Ismail, S. Double-pulse 2-μm integrated path differential absorption lidar airborne validation for atmospheric carbon dioxide measurement. *Appl. Opt.* **2016**, *55*, 4232–4246. https://doi.org/10.1364/AO.55.004232.
91. Zhu, Y.; Yang, J.; Chen, X.; Zhu, X.; Zhang, J.; Li, S.; Sun, Y.; Xia, H.; Bi, D.-C.; Bu, L.; et al. Airborne Validation Experiment of 1.57-μm Double-Pulse IPDA LIDAR for Atmospheric Carbon Dioxide Measurement. *Remote Sens.* **2020**, *12*, 1999. https://doi.org/10.3390/rs12121999.
92. Zhu, Y.; Yang, J.; Zhang, X.; Liu, J.; Zhu, X.; Zang, H.; Xia, T.; Fan, C.; Chen, X.; Sun, Y.; et al. Performance Improvement of Spaceborne Carbon Dioxide Detection IPDA LIDAR Using Linearty Optimized Amplifier of Photo-Detector. *Remote Sens.* **2021**, *13*, 2007. https://doi.org/10.3390/rs13102007.
93. Higdon, S.; Browell, E.; Ponsardin, P.; Grossmann, B.; Butler, C.; Chyba, T.; Mayo, M.; Allen, R.; Heuser, A.; Grant, W.; et al. Airborne differential absorption lidar system for measurements of atmospheric water vapor and aerosols. *Appl. Opt.* **1994**, *33*, 6422–6438. https://doi.org/10.1364/AO.33.006422.
94. Moore, A.; Brown, K.; Hall, W.; Barnes, J.; Edwards, W.; Petway, L.; Little, A.; Luck, W.; Jones, I.; Antill, C.; et al. Development of the Lidar Atmospheric Sensing Experiment (LASE)—An Advanced Airborne DIAL Instrument. In *Atmospheric Remote Sensing with Lidar*; Springer: Berlin/Heidelberg, Germany, 1996. https://doi.org/10.1007/978-3-642-60612-0_69.
95. Weckwerth, T.M.; Parsons, D.B.; Koch, S.E.; Moore, J.A.; LeMone, M.A.; Demoz, B.B.; Flamant, C.; Geerts, B.; Wang, J.; Feltz, W.F. An Overview of the International H_2O Project (IHOP_2002) and Some Preliminary Highlights. *Bull. Am. Meteorol. Soc.* **2004**, *85*, 253–278. https://doi.org/10.1175/BAMS-85-2-253.
96. Browell, E.V.; Ismail, S.; Hall, W.M.; Moore, A.S.; Kooi, S.A.; Brackett, V.G.; Clayton, M.B.; Barrick, J.D.W.; Schmidlin, F.J.; Higdon, N.S.; et al. LASE validation experiment. In *Advances in Atmospheric Remote Sensing with Lidar*; Springer Verlag: Berlin/Heidelberg, Germany, 1997; pp. 289–295.
97. Poberaj, G.; Fix, A.; Assion, A.; Wirth, M.; Kiemle, C.; Ehret, G. Airborne all-solid-state DIAL for water vapour measurements in the tropopause region: System description and assessment of accuracy. *Appl. Phys. B* **2002**, *B75*, 165–172. https://doi.org/10.1007/s00340-002-0965-x.
98. Bruneau, D.; Quaglia, P.; Flamant, C.; Meissonnier, M.; Pelon, J. Airborne lidar LEANDRE II for water-vapor profiling in the troposphere. *Appl. Opt.* **2001**, *40*, 3450–3475. https://doi.org/10.1364/AO.40.003450.
99. Machol, J.; Ayers, T.; Schwenz, K.; Koenig, K.; Hardesty, R.; Senff, C.; Krainak, M.; Abshire, J.; Bravo, H.; Sandberg, S. Preliminary measurements with an automated compact differential absorption lidar for the profiling of water vapor. *Appl. Opt.* **2004**, *43*, 3110–3121. https://doi.org/10.1364/AO.43.003110.
100. Mead, P.F.; DeYoung, R.J. A Water Vapor Differential Absorption LIDAR Design for Unpiloted Aerial Vehicles. NASA Tech. Memo. 2004, NASA/TM-2004-213507. Available online: https://ntrs.nasa.gov/api/citations/20050019540/downloads/20050019540.pdf (accessed on 15 November 2026).
101. Wirth, M.; Fix, A.; Mahnke, P.; Schwarzer, H.; Schrandt, F.; Ehret, G. The airborne multi-wavelength water vapor differential absorption lidar WALES: System design and performance. *Appl. Phys. B* **2009**, *96*, 201–213. https://doi.org/10.1007/s00340-009-3365-7.
102. Kiemle, C.; Schäfler, A.; Wirth, M.; Fix, A.; Rahm, S. Detection and Analysis of Water Vapor Transport by Airborne Lidars. *IEEE J. Sel. Top. Appl. Earth Obs. Remote Sens.* **2013**, *6*, 1189–1193. https://doi.org/10.1109/JSTARS.2013.2239609.
103. Refaat, T.; Singh, U.; Yu, J.; Petros, M.; Ismail, S.; Kavaya, M.; Davis, K. Evaluation of an airborne triple-pulsed 2 μm IPDA lidar for simultaneous and independent atmospheric water vapor and carbon dioxide measurements. *Appl. Opt.* **2015**, *54*, 1387–1398. https://doi.org/10.1364/AO.54.001387.

104. Refaat, T.F.; Petros, M.; Singh, U.N.; Antill, C.W.; Wong, T.-H.; Remus, R.; Reithmaier, K.; Lee, J.; Bowen, S.; Taylor, B.; et al. Airborne, direct-detection, 2-um triple-pulse IPDA lidar for simultaneous and independent atmospheric water vapor and carbon dioxide active remote sensing. *Proc. SPIE* **2018**, *10779*, 1077902. https://doi.org/10.1117/12.2324785.
105. Available online: https://airbornescience.nasa.gov/instrument/High_Altitude_Lidar_Observatory (accessed on 15 November 2026).
106. Carroll, B.J.; Nehrir, A.R.; Kooi, S.A.; Collins, J.E.; Barton-Grimley, R.A.; Notari, A.; Harper, D.B.; Lee, J. Differential absorption lidar measurements of water vapor by the High Altitude Lidar Observatory (HALO): Retrieval framework and first results. *Atmos. Meas. Tech.* **2022**, *15*, 605–626. https://doi.org/10.5194/amt-15-605-2022.
107. Bedka, K.M.; Nehrir, A.R.; Kavaya, M.; Barton-Grimley, R.; Beaubien, M.; Carroll, B.; Collins, J.; Cooney, J.; Emmitt, G.D.; Greco, S.; et al. Airborne lidar observations of wind, water vapor, and aerosol profiles during the NASA Aeolus calibration and val idation (Cal/Val) test flight campaign. *Atmos. Meas. Tech.* **2021**, *14*, 4305–4334. https://doi.org/10.5194/amt-14-4305-2021.
108. Available online: https://cordis.europa.eu/project/id/821868 (accessed on 15 November 2026).
109. Dherbecourt, J.B.; Raybaut, M.; Melkonian, J.M.; Hamperl, J.; Santagata, R.; Dalin, M.; Lebat, V.; Godard, A.; Flamant, C.; Totems, J.; et al. Design and pre-development of an airborne multi-species differential absorption Lidar system for water vapor and HDO isotope, carbon dioxide, and methane observation. *Proc. SPIE* **2021**, *11852*, 118521U. https://doi.org/10.1117/12.2599326.
110. World Meteorological Organization. The State of Greenhouse Gases in the Atmosphere Based on Global Observations through 2021. In *WMO Greenhouse Gas Bulletin*; World Meteorological Organization: Geneva, Switzerland, 2022; No.18. Available online: https://wmo.int/publication-series/wmo-greenhouse-gas-bulletin-no-18 (accessed on 15 November 2026).
111. World Meteorological Organization. The State of Greenhouse Gases in the Atmosphere Based on Global Observations through 2024. In *WMO Greenhouse Gas Bulletin*; World Meteorological Organization: Geneva, Switzerland, 2025; No.21. Available online: https://wmo.int/publication-series/wmo-greenhouse-gas-bulletin-no-21 (accessed on 15 November 2026).
112. Turner, A.J.; Frankenberg, C.; Kort, E.A. Interpreting contemporary trends in atmospheric methane. *Proc. Natl. Acad. Sci. USA* **2019**, *116*, 2805–2813. https://doi.org/10.1073/pnas.1814297116.
113. Degtiarev, E.V.; Geiger, A.R.; Richmond, R.D. Compact mid-infrared DIAL lidar for ground-based and airborne pipeline monitoring. *Proc. SPIE* **2003**, *4882*, 432–441. https://doi.org/10.1117/12.462573.
114. Riris, H.; Numata, K.; Li, S.; Wu, S.; Ramanathan, A.; Dawsey, M.; Mao, J.; Kawa, R.; Abshire, J. Airborne measurements of atmospheric methane column abundance using a pulsed integrated-path differential absorption lidar. *Appl. Opt.* **2012**, *51*, 8296–8305. https://doi.org/10.1364/AO.51.008296.
115. Riris, H.; Numata, K.; Wu, S.; Gonzalez, B.; Rodriguez, M.; Scott, V.; Kawa, S.; Mao, J. Methane optical density measurements with an integrated path differential absorption lidar from an airborne platform. *J. Appl. Remote Sens.* **2017**, *11*, 034001. https://doi.org/10.1117/1.JRS.11.034001.
116. Galkowski, M.; Jordan, A.; Rothe, M.; Marshall, J.; Koch, F.-T.; Chen, J.; Agusti-Panareda, A.; Fix, A.; Gerbig, C. In situ observations of greenhouse gases over Europe during the CoMet 1.0 campaign aboard the HALO aircraft. *Atmos. Meas. Tech.* **2021**, *14*, 1525–1544. https://doi.org/10.5194/amt-14-1525-2021.
117. Fiehn, A.; Kostinek, J.; Eckl, M.; Harlass, T.; Galkowski, M.; Chen, J.; Gerbig, C.; Röckmann, T.; Maazallahi, H.; Schmidt, M.; et al. Estimating CH_4, CO_2 and CO emissions from coal mining and industrial activities in the Upper Silesian Coal Basin using an aircraft-based mass balance approach. *Atmos. Chem. Phys.* **2020**, *20*, 12675–12695. https://doi.org/10.5194/acp-20-12675-2020.
118. Nickl, A.L.; Mertens, M.; Roiger, A.; Fix, A.; Amediek, A.; Fiehn, A.; Gerbig, C.; Galkowski, M.; Kerkweg, A.; Klausner, T.; et al. Hindcasting and forecasting of regional methane from coal mine emissions in the Upper Silesian Coal Basin using the online nested global regional chemistry-climate model MECO(n) (MESSy v2.53). *Geosci. Model Dev.* **2020**, *13*, 1925–1943. https://doi.org/10.5194/gmd-13-1925-2020.
119. Kostinek, J.; Roiger, A.; Eckl, M.; Fiehn, A.; Luther, A.; Wildmann, N.; Harlass, T.; Fix, A.; Knote, C.; Stohl, A.; et al. Estimating Upper Silesian coal mine methane emissions from airborne in situ observations and dispersion modeling. *Atmos. Chem. Phys.* **2021**, *21*, 8791–8807. https://doi.org/10.5194/acp-21-8791-2021.
120. Davis, K.J.; Browell, E.V.; Feng, S.; Lauvaux, T.; Obland, M.D.; Pal, S.; Baier, B.C.; Baker, D.F.; Baker, I.T.; Barkley, Z.R.; et al. The Atmospheric Carbonand Transport (ACT) America Mission. *Bull. Am. Meteorol. Soc.* **2021**, *102*, E1714–E1734. https://doi.org/10.1175/BAMS-D-20-0300.1.
121. Barton-Grimley, R.A.; Nehrir, A.R.; Kooi, S.A.; Collins, J.E.; Harper, D.; Notari, A.; Lee, J.; DiGangi, J.P.; Choi, Y.; Davis, K. Evaluation of the High Altitude Lidar Observatory (HALO) methane retrievals during the summer 2019 ACT-America campaign. *Atmos. Meas. Tech.* **2022**, *15*, 4623–4650. https://doi.org/10.5194/amt-15-4623-2022.

122. Cezard, N.; Valla, M.; Lombard, L.; Goular, D.; Augère, B.-T.; Dolfi-Bouteyre, A.; Fix, A.; Quatrevalet, M.; Bès, C.; Crevoisier, C. Double-Lidar airborne mission over Scandinavia for atmospheric transport assessment of CH_4 and CO_2. In Proceedings of the International Laser Radar Conference, Online, USA, 26 June–1 July 2022; p. S07_O03. Available online: https://hal.science/hal-03769242/file/DOTA22060.1644842175.pdf (accessed on 15 November 2026).
123. Bell, C.; Rutherford, J.; Brandt, A.; Sherwin, E.; Vaughn, T.; Zimmerle, D. Single-blind determination of methane detection limits and quantification accuracy using aircraft-based LiDAR. *Elem. Sci. Anthr.* **2022**, *10*, 00080. https://doi.org/10.1525/elementa.2022.00080.
124. Bridger Photonics. *The Emissions Impact of Gas Mapping LiDAR Scans Compared to the Emissions Detected*; Bridger Photonics: Bozeman, MT, USA, 2025. Available online: https://www.bridgerphotonics.com/blog/emissions-impact-gas-mapping-lidar-scans-compared-emissions-detected (accessed on 15 November 2026).
125. Kunkel, W.M.; Donahue, C.P.; Altamura, D.T.; Dudiak, C.; Moscona-Remnitz, B.; Goldsworth, N.C.; Kennedy, B.; Thorpe, M.J. Aerial Gas Mapping Lidar for Methane Emission Source Localization, Quantification, and Large-Scale Statistical Characterization. In *Proceedings of the Conference on Lasers and Electro-Optics*; Technical Digest Series; Optica Publishing Group: Washington, DC, USA, 2024; ATh1E.6. https://doi.org/10.1364/CLEO_AT.2024.ATh1E.6.
126. Romanovskii, O.A.; Sadovnikov, S.A.; Yakovlev, S.V.; Tuzhilkin, D.A.; Kharchenko, O.V.; Kravtsova, N.S. Mobile 3.4–μm differential absorption lidar system for remote sensing of the atmospheric methane. *Proc. SPIE* **2021**, *11916*, 119161T. https://doi.org/10.1117/12.2600547.
127. Romanovskii, O.A.; Sadovnikov, S.A.; Kharchenko, O.V.; Yakovlev, S.V. Remote Analysis of Methane Concentration in the Atmosphere with an IR Lidar System in the 3300–3430 nm Spectral Range. *Atmos. Ocean. Opt.* **2020**, *33*, 188–194. https://doi.org/10.1134/S1024856020020074.
128. Sadovnikov, S.; Romanovskii, O.; Yakovlev, S.; Kharchenko, O.; Kravtsova, N. Calibration and field test of mobile lidar for remote sensing of atmospheric methane. *J. Opt. Technol.* **2022**, *89*, 320–326. https://doi.org/10.1364/JOT.89.000320.
129. Yakovlev, S.V.; Romanovskii, O.A.; Sadovnikov, S.A.; Tuzhilkin, D.A.; Nevzorov, A.A.; Kharchenko, O.V.; Kravtsova, N.S. Mobile mid-infrared differential absorption lidar for methane monitoring in the atmosphere: Calibration and first in situ tests. *Results Opt.* **2022**, *8*, 100233. https://doi.org/10.1016/j.rio.2022.100233.
130. Available online: https://solar-laser.com/ (accessed on 15 November 2026).
131. Yakovlev, S.V.; Romanovskii, O.A.; Sadovnikov, S.A. Mobile Airborne Lidar for Remote Methane Monitoring: Design, Simulation of Atmospheric Measurements and First Flight Tests. *Remote Sens.* **2022**, *14*, 6355. https://doi.org/10.3390/rs14246355.
132. Lv, L.; Xiang, Y.; Wang, J.; Pan, Y.; Wang, Z.; Yi, Z.; Zhang, T.; Liu, W. Shipborne lidar measurements of ozone over the southeastern coastal regions of China in winter. *Environ. Res.* **2025**, *272*, 121165. https://doi.org/10.1016/j.envres.2025.121165.
133. Liu, P.; Zhang, T.; Sun, X.; Fan, G.; Xiang, Y.; Fu, Y.; Dong, Y. Compact and movable ozone differential absorption lidar system based on an all-solid-state, tuning-free laser source. *Opt. Express* **2020**, *28*, 13786–13800. https://doi.org/10.1364/OE.391333.
134. Browell, E.V.; Ismail, S.; Grant, W.B. Differential absorption lidar (DIAL) measurements from air and space. *Appl. Phys. B.* **1998**, *67*, 399–410. https://doi.org/10.1007/s003400050523.
135. Langford, A.; Senff, C.; Alvarez, II; Banta, R.; Hardesty, R.; Parrish, D.; Ryerson, T. Comparison between the TOPAZ Airborne Ozone Lidar and In Situ Measurements during TexAQS 2006. *J. Atmos. Ocean. Technol.* **2011**, *28*, 1243–1257. https://doi.org/10.1175/JTECH-D-10-05043.1.
136. Available online: https://csl.noaa.gov/groups/csl3/instruments/topaz/ (accessed on 15 November 2026).
137. Alvarez, R.J.; Senff, C.J.; Langford, A.O.; Weickmann, A.M.; Law, D.C.; Machol, J.L.; Merritt, D.A.; Marchbanks, R.D.; Sandberg, S.P.; Brewer, W.A. Development and Application of a Compact, Tunable, Solid-State Airborne Ozone Lidar System for Boundary Layer Profiling. *J. Atmos. Ocean. Technol.* **2011**, *28*, 1258–1272. https://doi.org/10.1175/jtech-d-10-05044.1.
138. Alvarez, R.J.; Senff, C.J.; Langford, A.O.; Weickmann, A.M.; Sandberg, S.P.; Marchbanks, R.D.; Brewer, W.A.; Hardesty, R.M. Reconfiguration of the NOAA TOPAZ Lidar for Ground-based Measurement of Ozone and Aerosol Backscatter. 26th International Laser Radar Conference, Porto Heli, Greece, 25–29 June 2012; Volume 2012, pp. 249–252.
139. Seabrook, J.; Whiteway, J.; Gray, L.; Staebler, R.; Herber, A. Airborne lidar measurements of surface ozone depletion over Arctic sea ice. *Atmos. Chem. Phys.* **2013**, *13*, 6023–6029. https://doi.org/10.5194/ACP-13-6023-2013.
140. Hair, J.; Hostetler, C.; Cook, A.; Harper, D.; Notari, A.; Fenn, M.; Newchurch, M.; Wang, L.; Kuang, S.; Knepp, T.; et al. New capability for ozone DIAL profiling measurements in the troposphere and lower stratosphere from aircraft. *EPJ Web Conf.* **2018**, *176*, 01006. https://doi.org/10.1051/epjconf/201817601006.

141. Fix, A.; Steinebach, F.; Wirth, M.; Schäfler, A.; Ehret, G. Development and application of an airborne differential absorption lidar for the simultaneous measurement of ozone and water vapor profiles in the tropopause region. *Appl. Opt.* **2019**, *58*, 5892–5900. https://doi.org/10.1364/AO.58.005892.
142. Remsberg, E.; Gordley, L. Analysis of differential absorption lidar from the Space Shuttle. *Appl. Opt.* **1978**, *17*, 624–630. https://doi.org/10.1364/AO.17.000624.
143. National Aeronautics and Space Administration. Shuttle Atmospheric Lidar Research Program. In *Final Report of Atmospheric Lidar Working Group*; National Aeronautics and Space Administration: Washington, DC, USA, 1979; NASA SP-433, 226 p. Available online: https://ntrs.nasa.gov/api/citations/19800003166/downloads/19800003166.pdf (accessed on 15 November 2026).
144. Winker, D.M.; Couch, R.H.; McCormick, M.P. An overview of LITE: NASA's Lidar In-space Technology Experiment. *Proc. IEEE* **1996**, *84*, 164–180. https://doi.org/10.1109/5.482227.
145. Balin, Y.S.; Tikhomirov, A.A. The history of development and operaion of the first Russian space lidar BALKAN integrated into Mir space station. *Opt. Atmos. I Okeana* **2011**, *24*, 1078–1087.
146. Chanin, M.-L.; Hauchecorne, A.; Malique, C.; Nedeljkovic, D.; Blamont, J.E.; Desbois, M.; Tulinov, G.; Melnikov, V. First results of the ALISSA lidar on board the MIR platform. *Comptes Rendus Acad. Sci. Ser. II Fasc. A-Sci. Terre Planetes* **1999**, *328*, 359–366.
147. Singh, U.N.; Tzeremes, G.; Refaat, T. F.; Ribes Pleguezuelo, P. (Eds.) Space-based Lidar Remote Sensing Techniques and Emerging Technologies. In *Proceedings of the 3rd International Space Lidar Workshop*; Springer: Cham, Switzerland, 2024; ISBN 978-3-031-53617-5. https://doi.org/10.1007/978-3-031-53618-2.
148. Available online: https://cce.nasa.gov/ascends/ (accessed on 15 November 2026).
149. Available online: https://cce.nasa.gov/ascends/12-30-08%20ASCENDS_Workshop_Report%20clean.pdf (accessed on 15 November 2026).
150. Abshire, J.B.; Riris, H.; Allan, G.R.; Weaver, C.J.; Mao, J.; Sun, X.; Hasselbrack, W.E.; Yu, A.W.; Amediek, A.; Choi, Y.; et al. A lidar approach to measure CO_2 concentrations from space for the ASCENDS Mission. *Proc. SPIE* **2010**, *7832*, 78320D. https://doi.org/10.1117/12.868567.
151. Kawa, S.; Mao, J.; Abshire, J.; Collatz, G.; Sun, X.; Weaver, C. Simulation studies for a space-based CO_2 lidar mission. *Tellus B* **2010**, *62*, 759–769. https://doi.org/10.1111/j.1600-0889.2010.00486.x.
152. Caron, J.; Durand, Y.; Bezy, J.-L.; Meynart, R. Performance modeling for A-SCOPE: A space-borne lidar measuring atmospheric CO_2. *Proc. SPIE* **2009**, *7479*, 74790E. https://doi.org/10.1117/12.830364.
153. Allan, G.; Sun, X.; Mao, J.; Kawa, R.; Riris, H.; Abshire, J.; Hasselbrack, W.; Rodriguez, M.; Weaver, C.; Li, S.; et al. LIDAR technology for measuring trace gases on Mars and Earth. *Proc. SPIE* **2017**, *10565*, 105650G. https://doi.org/10.1117/12.2309207.
154. Riris, H.; Numata, K.; Li, S. Lidar technology for measuring trace gases on Mars and Earth. *Proc. SPIE* **2011**, *8192*, 819203.
155. Ehret, G.; Bousquet, P.; Pierangelo, C.; Alpers, M.; Millet, B.; Abshire, J.; Bovensmann, H.; Chevallier, F.; Ciais, P.; Crevoisier, C.; et al. MERLIN: A French-German space lidar mission dedicated to atmospheric methane. *Remote Sens.* **2017**, *9*, 1052. https://doi.org/10.3390/rs9101052.
156. Pierangelo, C.; Millet, B.; Esteve, F.; Alpers, M.; Ehret, G.; Flamant, P.; Berthier, S.; Gibert, F.; Chomette, O.; Edouart, D.; et al. MERLIN (Methane Remote Sensing Lidar Mission): An Overview. *EPJ Web Conf.* **2016**, *119*, 26001. https://doi.org/10.1051/epjconf/201611926001.
157. Nikolov, S.; Wuehrer, C.; Kühl, C.; Bode, M.; Hupfer, W.; Lucarelli, S. MERLIN: Design of an IPDA LIDAR instrument. *CEAS Space J.* **2019**, *11*, 437–457. https://doi.org/10.1007/s12567-019-00267-7.
158. Kiemle, C.; Ehret, G.; Amediek, A.; Fix, A.; Quatrevalet, M.; Wirth, M. Potential of Spaceborne Lidar Measurements of Carbon Dioxide and Methane Emissions from Strong Point Sources. *Remote Sens.* **2017**, *9*, 1137. https://doi.org/10.3390/rs9111137.
159. Wang, S.; Ke, J.; Chen, S.; Zheng, Z.; Cheng, C.; Tong, B.; Liu, J.; Liu, D.; Chen, W. Performance Evaluation of Spaceborne Integrated Path Differential Absorption Lidar for Carbon Dioxide Detection at 1572 nm. *Remote Sens.* **2020**, *12*, 2570. https://doi.org/10.3390/rs12162570.

160. Chen, W.; Liu, J.; Hou, X.; Zang, H.; Wan, Y.; Zhu, X.; Ma, X.; Chen, D.; Li, R. Spaceborne Aerosol and Carbon Dioxide Detection Lidar (ACDL) Status and Progress. In *Space-Based Lidar Remote Sensing Techniques and Emerging Technologies LIDAR 2023*; Springer Aerospace Technology; Singh, U.N., Tzeremes, G., Refaat, T.F., Ribes Pleguezuelo, P., Eds.; Springer: Cham, Switzerland, 2024. https://doi.org/10.1007/978-3-031-53618-2_9.
161. Chen, C.; Fan, C.; Wu, Z.; Xie, Y.; Hu, J.; Yang, J.; Zhu, X.; Liu, J.; Chen, W. Measurement of the global surface reflectance at 1572 nm using spaceborne aerosol and carbon dioxide detection lidar. *Appl. Phys. B* **2025**, *131*, 109. https://doi.org/10.1007/s00340-025-08473-4.

Disclaimer/Publisher's Note: The statements, opinions and data contained in all publications are solely those of the individual author(s) and contributor(s) and not of MDPI and/or the editor(s). MDPI and/or the editor(s) disclaim responsibility for any injury to people or property resulting from any ideas, methods, instructions or products referred to in the content.